UNIVERSITEIT ANTWERPEN

Faculteit Wetenschappen

Departement Fysica

Vortex Structure in a Mesoscopic Superconducting Sphere

Eindverhandeling ingediend tot het bekomen van de meestergraad
nanofysica

Dong Sun

Promotor: Prof. dr. F. M. Peeters
Co-promotor: Dr. Ben Baelus

Academiejaar 2005-2006
Antwerpen

ACKNOWLEDGMENTS

I would like to start this thesis by paying tribute to those people who have greatly helped me on my thesis work.

My gratitude and appreciation go to Prof. F. M. Peeters who has accepted to be the Promotor of my advanced master thesis, prepared me such an interesting research topic and provided me with great and invaluable support and guidance. It has been an important and wonderful experience for me to work in the excellent research group under his leadership.
I am also extremely grateful to my co-promotor Dr. B. Baelus, whose knowledge and patience have largely helped me in solving most of the problems encountered during writing this thesis. I thank him too for his great guidance in showing me in detail the application of many scientific calculation softwares.

My great thanks also go to Prof. B. Partoens, Dr. M. Milosevic and PHD-candidates An, Yosyp, and Roeland. I thank them for their help in answering my academic questions and in solving many problems regarding software application.

Furthermore, I strongly feel the necessity to thank all the Professors who have given me class during my study at University Antwerp, for their valuable instruction, helpful advice and critical evaluation.

Dong Sun
Antwerpen-2006

Contents

1

Introduction

The recently rapid miniaturization of electronic circuits requires smaller electrical components. Because of their excellent electronic and magnetic properties, superconductors may become one of the possible candidates to emerge after the silicon area. However, in order to achieve this, it is necessary to learn how individual superconducting elements of prospective circuites will operate.

It is known that the electric and magnetic properties of superconductors are largely influenced by the boundary conditions, or the sample size which can be comparable with the characteristic length scales. Therefore new physical phenomena can be expected in mesoscopic superconductor samples having dimensions of the same order as the coherence length ξ or the magnetic penetration depth λ.

Based on recent experimental discoveries in mesoscopic superconductors, in this thesis we will investigate theoretically the vortex structure in a mesoscopic sphere placed in a homogenous magnetic field. We only consider the situation of a sphere surrounded by a vacuum boundary in space. The initial step of this study was done earlier in the group of Peeters by Schweigert, and others. They studied single mesoscopic superconducting disks and found that the vortex configuration and the critical parameters depend on the sample geometry. We will adjust their formalism to investigate the effect of the size of the sphere on the vortex structure of the superconductor. We need to mention that for this research topic, Du [10][15] has already done numerical work based on the Ginzburg-Landau theory for superconductors. He exploited the finite element and finite difference and finite volume techniques and obtained the distribution of the Cooper-pair density and the vortex structure in three dimension space. In our work, we will use a different approach based on

the expansion of the order parameter in solutions of the linearized Ginzburg-Landau equation. We will focus on the the stability of the vortex and the transition between the giant and multi-vortex states.

This thesis is composed of five chapters:

Chapter 1 gives a short introduction of the history of superconductivity and related mesoscopic superconducting structures, and the corresponding theory. We present a derivation of the GL equations, which are the core theoretical framework of this thesis. Type-I and type-II superconductors and the character lengths are introduced. The properties of a giant vortex and a multi-vortex are also discussed.

Chapter 2 gives one theoretical model for the mesoscopic superconducting sphere. The free energy of the different vortex states and the stability criterion for both the giant vortex and the multi-vortex states are obtained.

Chapter 3 shows the theoretical results about the giant vortex in a superconducting sphere. We obtained the eigenvalue, the order parameter and the free energy of the giant vortex for different vorticities and radius of the sphere. The dependence of the order parameter on the magnetic field are also shown. Besides the ground states, we also investigated the Cooper-pair density and the free energy of excited states, which are later proved to be not stable in our mesoscopic sphere.

Chapter 4 shows the corresponding theoretical results on the multi-vortex states, in which we obtain the stability and the order parameter of the multi-vortex states. The transition between giant vortex and multi-vortex states are also found.

Chapter 5 gives the conclusion, in which we will summarize the most important results of this thesis.

1.1 HISTORICAL SURVEY OF SUPERCONDUCTIVITY

The superconductivity was first discovered in 1911 at the Leiden laboratory, by Heike Kamerlingh Onnes, who first liquified helium. He was awarded the Nobel prize in 1913. He studied the electrical resistance of many substances at liquid helium temperature, when he noticed that the resistance of mercury dropped sharply to zero at a critical temperature of 4.2K [see Fig. 1.1]. The same properties were observed in some other metals, such as lead and tin. This new phenomenon was the so called *superconductivity*.

Before 1933, it was considered that superconductivity was just perfect conductivity. In 1933, Meissner and Ochsenfeld found that the magnetic field is expelled from an originally normal sample when it is cooled through the critical temperature [see Fig. 1.2] [4]. This is called the Meissner effect.

Only after 20 years since the discovery of superconductivity, the first theory about superconducting was brought forward. In 1935, the brothers London provided the first phenomenological theory describing the superconducting mechanism, which were proven to be valid in describing the superconduct-

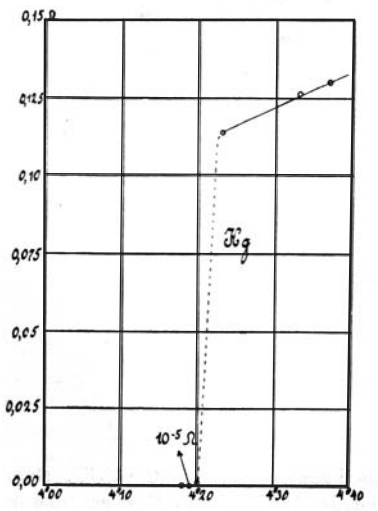

Fig. 1.1 Resistance in Ohm of a specimen of mercury versus absolute temperature. This plot of Kamerlingh Onnes marked the discovery of superconductivity. [From Ref. [16].]

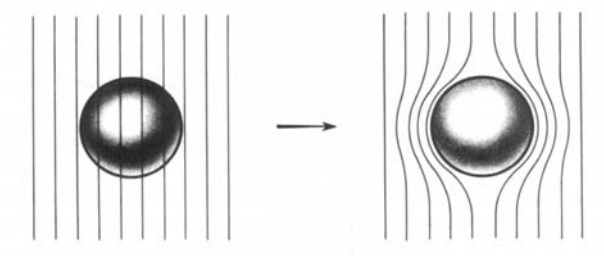

Fig. 1.2 Meissner effect in a superconducting sphere cooled in a constant applied magnetic field. On passing below the transition temperature, the lines of induction are ejected from the sphere. [From Ref. [16].]

ing behavior and vortex states in extreme type-II superconductors. However, the London theory treats vortices as points and do not take into account the finite size and the inner structure of the vortex. A new phenomenological theory was developed by Ginzburg and Landau in 1950, the so-called Ginzburg-Landau theory, in which quantum mechanics is introduced into the theory and described the spatial distribution of superconducting electrons. But the microscopic mechanism of superconductivity was finally advanced by Bardeen, Cooper and Schrieffer in 1957 with the famous BCS theory, by which they were awarded the Nobel prize for physics in 1972. In 1958, Gor'kov found a microscopic interpretation for all phenomenological parameters of the

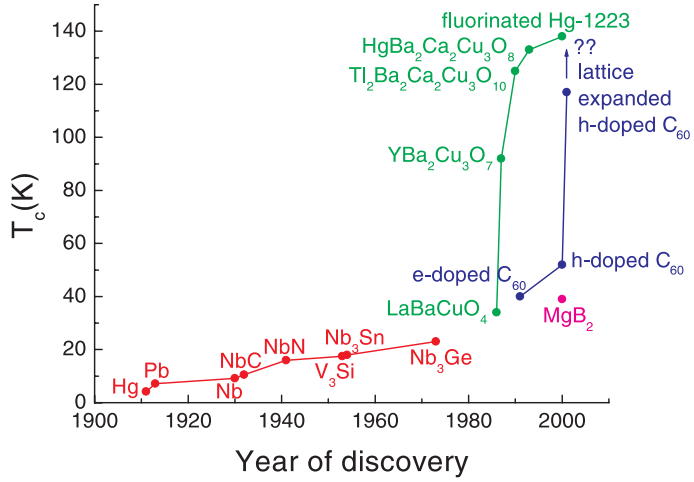

Fig. 1.3 The critical temperature T_c versus the year of discovery. Red represents the low T_c superconductors, green the cuprates, blue the fullerenes and magenta MgB_2.

Ginzburg-Landau theory [9], and derived the range of applicability of the GL theory.

In 1986, Bednorz and Müller discovered the first high-T_c superconductor [11] with T_c of 38K. Before this discovery the highest critical temperature was only 23K for Nb_3Ge. For this discovery, Bednorz and Müller obtained the Nobel prize in 1987. Subsequently different cuprates have been found with increasing critical temperature. By 1993, cuprates with a T_c of 133K at atmospheric pressure were found ($HgBa_2Ca_2Cu_3O_8$) [12], and in 2000, a slight increase in the transition temperature was detected for fluorinated Hg-1223 samples ($T_c = 138$K) [14].

But the development of theory does not keep up with new experiment discoveries. Up to now, the theories were not able to describe many properties of the high-T_c materials. The electron-phonon mechanism became questionable. New mechanisms, such as the so-called d-wave pairing, has been proposed. But the reason for this high T_c values is still blurry.

1.1.1 Ginzburg-Landau theory

In 1950, Ginzburg and Landau proposed a new phenomenological theory taking into account quantum effects [23]. They introduced the wavefunction of superconducting electrons $\Psi(\vec{r})$ as a complex order parameter which is nonzero at $T < T_c$ and vanishes at $T \geq T_c$ (second order phase transition). This order parameter is related to the density of superconducting electrons n_s as $|\Psi(\vec{r})|^2 = n_s/2$.

The Ginzburg-Landau theory is based on Landau's theory of second-order phase transition [7] in which the free energy is expanded in powers of the order parameter. The derivation of the Ginzburg-Landau theory and its validity is described in full detail in section 1.3. Here, we just mention the two Ginzburg-Landau equations:

$$\alpha\Psi + \beta\left|\Psi\right|^2\Psi + \frac{1}{2m^*}\left(-i\hbar\overrightarrow{\nabla} - \frac{2e}{c}\overrightarrow{A}\right)^2\Psi = 0\ , \tag{1.1}$$

$$\vec{j}_S = -\frac{i\hbar e}{m^*}\left(\Psi^*\overrightarrow{\nabla}\Psi - \Psi\overrightarrow{\nabla}\Psi^*\right) - \frac{4e^2}{m^*c}\left|\Psi\right|^2\overrightarrow{A}\ , \tag{1.2}$$

where the superconducting current density $\vec{j}_S$ is given by the Maxwell equation

$$\vec{j}_S = \frac{c}{4\pi} rot\, rot\, \overrightarrow{A}\ . \tag{1.3}$$

In 1957, Abrikosov calculated the properties of bulk type-II superconductors (see section 1.4) with the Ginzburg-Landau theory and found the so-called mixed state where quantized units of magnetic flux penetrate in the superconductor in a regular array. This array of penetrating flux, which corresponds to the lowest energy configuration, is later called the Abrikosov vortex lattice.

With this theory it became possible to describe spatial distribution of superconducting electrons in type-I and type-II superconductors, taking into account the finite sizes of the vortices. This was impossible within the framework of the London theory.

1.1.2 BCS theory

Only 46 years after the discovery of superconductivity the microscopic mechanism of superconductivity was described by Bardeen, Cooper and Schrieffer in 1957 [13]. The vortex structure and the critical parameters can be precisely calculated using the Ginzburg-Landau theory.

The kernel of the BCS theory is the existence of a pair of electrons, the so-called Cooper-pair [17], which has a lower energy than two individual electrons. One electron slightly disturbs the nearest lattice. The resulting phonon interacts quickly with another electron, which takes advantage of the deformation and lowers its energy. The second electron emits a phonon by itself which interacts with the first electron and so on. It is that passing back and forth of phonons which couples the two electrons together and brings them into a lower energy state. The energy gap stabilizes the Cooper-pairs and prevents them from breaking apart. The scattering of the lattice atoms is eliminated because of the presence of the superconducting gap, which causes zero resistance. Electrons in such a Cooper-pair are situated on the Fermi surface and have opposite momentum and opposite spin. These electrons form a cloud of Cooper-pairs which drift cooperatively through the crystal.

In order to destroy one Cooper-pair, it is necessary to destroy all Cooper-pairs in a macroscopic region of a superconductor. It requires a lot of energy and, consequently, the probability of the process is very small. Thus, the superconducting state is an ordered state of conducting electrons.

In 1959 Gor'kov showed that the Ginzburg-Landau theory was just a limiting form of the BCS theory, valid near T_c and suitable to deal with spatially varying situations [21]. He showed that the order parameter Ψ can be seen as the wavefunction of the center-of-mass motion of the Cooper-pairs.

1.2 MESOSCOPIC SUPERCONDUCTIVITY

Mesoscopic superconductors are samples which have sizes comparable to the two characteristic length scales: the coherence length ξ or the magnetic penetration length λ.

While in bulk superconductors penetrating vortices form a triangular lattice due to the vortex-vortex repulsion and the critical parameters and the properties are determined by the material, in mesoscopic superconductors the situation is more complicated. In mesoscopic superconductors there is a competition between the triangular configuration of the vortex lattice and the boundary which tries to impose its geometry on the vortex lattice. Therefore, the properties of mesoscopic superconductors are very different compared to those of bulk superconductors. In this thesis we will investigate the influence of the sample boundary on the vortex configurations and the critical parameters for mesoscopic samples with different geometries.

1.3 DERIVATION OF THE GINZBURG-LANDAU THEORY

Based on the theory of second-order phase transitions developed by Landau, Ginzburg and Landau together developed a phenomenological theory [23], in which they assumed that the wavefunction of the superconducting electrons $\Psi(\overrightarrow{r})$ is the order parameter and they chose the normalization of this wavefunction such that $|\Psi(\overrightarrow{r})|^2$ gives the density of Cooper-pairs:

$$|\Psi(\overrightarrow{r})|^2 = n_s/2 \ , \tag{1.4}$$

where n_s is the density of the superconducting electrons.

The theory is based on an expansion of the free energy in powers of the order parameter, which is small close to the superconducting/normal transition at the critical temperature T_c. Thus it is explicit that the GL theory is only valid around T_c.

1.3.1 Free energy

The Gibbs free energy density closed to the critical temperature T_c can be expanded as [22]

$$G_s = G_n + \alpha \left|\Psi\right|^2 + \frac{\beta}{2}\left|\Psi\right|^4 + \frac{1}{2m^*}\left|\left(-i\hbar\overrightarrow{\nabla} - \frac{2e}{c}\overrightarrow{A}\right)\Psi\right|^2 + \frac{H^2}{8\pi} - \frac{\overrightarrow{H} - \overrightarrow{H}_0}{4\pi}\cdot\overrightarrow{H}_0 \ , \tag{1.5}$$

where H is the microscopic field at a given point of the superconductor and G_n is the free energy density of a superconductor in the normal state when no field is applied. When a magnetic field is applied, the free energy density of a superconductor in the normal state is given by $G_{nH} = G_n + H_0^2/8\pi$, where $H_0^2/8\pi$ is the magnetic energy density.

- The first part of Eq. (1.5) is the expansion of the free energy density for a homogeneous superconductor without applied magnetic field close to the zero-field critical temperature $T_{c0} \equiv T_c(H_0 = 0)$,

$$G_n + \alpha\left|\Psi\right|^2 + \frac{\beta}{2}\left|\Psi\right|^4 \ , \tag{1.6}$$

  in which α and β are characteristic coefficients of the material. The coefficient α is negative and depends on the temperature as $\alpha \propto (T - T_{c0})$, while β is a positive constant. From Eq. (1.6) the Cooper-pair density corresponding to the free energy minimum at temperatures below T_{c0} can be calculated as

$$\left|\Psi_0\right|^2 = -\alpha/\beta \ . \tag{1.7}$$

- The second term is the kinetic energy of the Cooper-pairs:

$$\frac{1}{2m^*}\left|\left(-i\hbar\overrightarrow{\nabla} - \frac{2e}{c}\overrightarrow{A}\right)\Psi\right|^2 \ , \tag{1.8}$$

  where the mass and the charge of a Cooper-pair m^* is equal to two individual electrons.

- The third term simply represents the magnetic energy density, i.e.

$$\frac{H^2}{8\pi} \ . \tag{1.9}$$

- The last term describes the reduction of the magnetic field due to the penetration of the field, i.e.

$$-\frac{\overrightarrow{H} - \overrightarrow{H}_0}{4\pi}\cdot\overrightarrow{H}_0 \ . \tag{1.10}$$

Without this term expression (1.4) would be the free energy F. For a superconductor in an external field, the energy that is a minimum at equilibrium is not the free energy F but the Gibbs free energy G which is defined as [19]:

$$G = F - \frac{\overrightarrow{H} - \overrightarrow{H}_0}{4\pi} \cdot \overrightarrow{H}_0 \ . \tag{1.11}$$

The overall Gibbs free energy of a superconductor is

$$\mathcal{G}_{sH} = \mathcal{G}_{nH} + \int \left\{ \alpha \left|\Psi\right|^2 + \frac{1}{2}\beta \left|\Psi\right|^4 + \frac{1}{2m^*} \left| \left(-i\hbar\overrightarrow{\nabla} - \frac{2e}{c}\overrightarrow{A} \right) \Psi \right|^2 + \frac{H^2}{8\pi} + \frac{H_0^2}{8\pi} - \frac{\overrightarrow{H} \cdot \overrightarrow{H}_0}{4\pi} \right\} dV \ , \tag{1.12}$$

where the integration is carried out over the entire space V. Minimizing $\mathcal{G}_{sH}$ with respect to $\Psi(\overrightarrow{r})$ and $\overrightarrow{A}(\overrightarrow{r})$ leads to the Ginzburg-Landau equations which will be derived below.

1.3.2 First Ginzburg-Landau equation

In order to obtain the minimum of the total Gibbs free energy, we vary expression (1.12) with respect to Ψ^* [22]:

$$\int \left\{ \alpha\Psi\delta\Psi^* + \beta\Psi \left|\Psi\right|^2 \delta\Psi^* + \frac{1}{2m^*} \overrightarrow{\varphi} \cdot \left(i\hbar\overrightarrow{\nabla} - \frac{2e}{c}\overrightarrow{A} \right) \delta\Psi^* \right\} dV' = 0 \ , \tag{1.13}$$

where

$$\overrightarrow{\varphi} = \left(-i\hbar\overrightarrow{\nabla} - \frac{2e}{c}\overrightarrow{A} \right) \Psi \ , \tag{1.14}$$

and V' is the sample volume. The integration is restricted to the volume V' because outside this region Ψ is zero. The last term of Eq. (1.13) equals

$$\frac{i\hbar}{2m^*} \int \overrightarrow{\varphi} \cdot \overrightarrow{\nabla}\delta\Psi^* dV' - \frac{2e}{2m^*c} \int \overrightarrow{\varphi} \cdot \overrightarrow{A}\delta\Psi^* dV' \ , \tag{1.15}$$

and can be simplified to

$$\frac{i\hbar}{2m^*} \left[- \int \delta\Psi^* \overrightarrow{\nabla} \cdot \overrightarrow{\varphi} dV' + \int \overrightarrow{\nabla} \cdot \left(\delta\Psi^* \overrightarrow{\varphi} \right) dV' \right] - \frac{2e}{2m^*c} \int \overrightarrow{\varphi} \cdot \overrightarrow{A}\delta\Psi^* dV' \ , \tag{1.16}$$

by making use of $\overrightarrow{\nabla} \cdot (\delta\Psi^* \overrightarrow{\varphi}) = \overrightarrow{\varphi} \cdot \overrightarrow{\nabla}\delta\Psi^* + \delta\Psi^* \overrightarrow{\nabla} \cdot \overrightarrow{\varphi}$.

Substituting Eq. (1.16) in Eq. (1.13) results in

$$\int \left\{ \alpha\Psi\delta\Psi^* + \beta\Psi \left|\Psi\right|^2 \delta\Psi^* - \frac{i\hbar}{2m^*} \delta\Psi^* \overrightarrow{\nabla} \cdot \overrightarrow{\varphi} + \frac{i\hbar}{2m^*} \overrightarrow{\nabla} \cdot \left(\delta\Psi^* \overrightarrow{\varphi} \right) - \frac{2e}{2m^*c} \overrightarrow{\varphi} \cdot \overrightarrow{A}\delta\Psi^* \right\} dV' = 0 \ . \tag{1.17}$$

Using Gauss theorem $\int \overrightarrow{\nabla} \cdot \overrightarrow{A} dV' = \oint \overrightarrow{n} \cdot \overrightarrow{A} dS'$ this can be rewritten as

$$\int \left\{ \alpha \Psi \delta \Psi^* + \beta \Psi \left| \Psi \right|^2 \delta \Psi^* - \frac{i\hbar}{2m^*} \delta \Psi^* \overrightarrow{\nabla} \cdot \overrightarrow{\varphi} - \frac{2e}{2m^* c} \overrightarrow{\varphi} \cdot \overrightarrow{A} \delta \Psi^* \right\} dV' + \frac{i\hbar}{2m^*} \oint_{S'} \overrightarrow{n} \cdot \delta \Psi^* \overrightarrow{\varphi} dS' = 0 \ , \tag{1.18}$$

where S' is the sample surface, and thus

$$\int \left\{ \alpha \Psi \delta \Psi^* + \beta \Psi \left| \Psi \right|^2 \delta \Psi^* - \frac{i\hbar}{2m^*} \delta \Psi^* \overrightarrow{\nabla} \cdot \overrightarrow{\varphi} - \frac{2e}{2m^* c} \overrightarrow{\varphi} \cdot \overrightarrow{A} \delta \Psi^* \right\} dV' = 0 \ , \tag{1.19}$$

and

$$\frac{i\hbar}{2m^*} \oint_{S'} \overrightarrow{n} \cdot \delta \Psi^* \overrightarrow{\varphi} dS' = 0 \ . \tag{1.20}$$

Substituting Eq. (1.14) into equations (1.18) and (1.19), and using $\overrightarrow{\nabla} \Psi \cdot \overrightarrow{A} = \overrightarrow{A} \cdot \overrightarrow{\nabla} \Psi + \left(\overrightarrow{\nabla} \cdot \overrightarrow{A} \right) \Psi = \overrightarrow{A} \cdot \overrightarrow{\nabla} \Psi$ since $\overrightarrow{\nabla} \cdot \overrightarrow{A} = 0$ we find

$$\int \left\{ \alpha \Psi \delta \Psi^* + \beta \Psi \left| \Psi \right|^2 \delta \Psi^* - \frac{1}{2m^*} \left(-i\hbar \overrightarrow{\nabla} - \frac{2e}{c} \overrightarrow{A} \right)^2 \Psi \delta \Psi^* \right\} dV' = 0 \ , \tag{1.21}$$

and

$$\frac{i\hbar}{2m^*} \oint_{S'} \overrightarrow{n} \cdot \delta \Psi^* (-i\hbar \overrightarrow{\nabla} - \frac{2e}{c} \overrightarrow{A}) \Psi dS' = 0 \ . \tag{1.22}$$

As expressions (1.21) and (1.22) must be valid for an arbitrary function $\delta \Psi^*$, we obtain the first equation of the Ginzburg-Landau theory and its boundary condition:

$$\alpha \Psi + \beta \left| \Psi \right|^2 \Psi + \frac{1}{2m^*} \left(-i\hbar \overrightarrow{\nabla} - \frac{2e}{c} \overrightarrow{A} \right)^2 \Psi = 0 \ , \tag{1.23}$$

$$\overrightarrow{n} \cdot (-i\hbar \overrightarrow{\nabla} - \frac{2e}{c} \overrightarrow{A}) \Psi \Big|_{boundary} = 0 \ , \tag{1.24}$$

where $\overrightarrow{n}$ is the unit vector normal to the surface of the superconductor.

1.3.3 Second Ginzburg-Landau equation

In order to obtain the minimum of the Gibbs free energy, we vary Eq. (1.12) with respect to $\overrightarrow{A}$ [22]:

$$\frac{1}{2m^*} \int \left[\left(-\frac{2e}{c} \delta \overrightarrow{A} \Psi^* \right) \cdot \left(-i\hbar \overrightarrow{\nabla} \Psi - \frac{2e}{c} \overrightarrow{A} \Psi \right) + \left(i\hbar \overrightarrow{\nabla} \Psi^* - \frac{2e}{c} \overrightarrow{A} \Psi^* \right) \cdot \left(-\frac{2e}{c} \delta \overrightarrow{A} \Psi \right) \right] dV + \frac{1}{4\pi} \int \left(rot \, \overrightarrow{A} - \overrightarrow{H}_0 \right) \cdot rot \, \delta \overrightarrow{A} dV = 0 \ , \tag{1.25}$$

with $\overrightarrow{H} = rot\,\overrightarrow{A}$, and V the volume of the entire space. The variation $\delta\left(\overrightarrow{H}\right)^2 = \delta\left(rot\,\overrightarrow{A}\right)^2$ has been written as $2\,rot\,\overrightarrow{A}\cdot rot\,\delta\overrightarrow{A}$. Using the formula $div\left[\overrightarrow{a}\times\overrightarrow{b}\right] = \overrightarrow{b}\cdot rot\,\overrightarrow{a} - \overrightarrow{a}\cdot rot\,\overrightarrow{b}$ and taking $\overrightarrow{b} = rot\,\overrightarrow{A} - \overrightarrow{H}_0$ and $\overrightarrow{a} = \delta\overrightarrow{A}$ we find

$$\frac{1}{2m^*}\int\left[\left(-\frac{2e}{c}\delta\overrightarrow{A}\Psi^*\right)\cdot\left(-i\hbar\overrightarrow{\nabla}\Psi - \frac{2e}{c}\overrightarrow{A}\Psi\right) + \left(i\hbar\overrightarrow{\nabla}\Psi^* - \frac{2e}{c}\overrightarrow{A}\Psi^*\right)\cdot\left(-\frac{2e}{c}\delta\overrightarrow{A}\Psi\right)\right]dV +$$
$$\frac{1}{4\pi}\int\left[\delta\overrightarrow{A}\cdot rot\,rot\,\overrightarrow{A} + div\left(\delta\overrightarrow{A}\times\left(rot\,\overrightarrow{A} - \overrightarrow{H}_0\right)\right)\right]dV = 0\ . \qquad (1.26)$$

After making use of Gauss's theorem the last part of Eq. (1.26) can be written as

$$\int div\left(\delta\overrightarrow{A}\times\left(rot\,\overrightarrow{A} - \overrightarrow{H}_0\right)\right)dV = \oint_S d\overrightarrow{S}\cdot\left[\delta\overrightarrow{A}\times\left(rot\,\overrightarrow{A} - \overrightarrow{H}_0\right)\right]\ , \qquad (1.27)$$

which is zero because S is the boundary of the entire space at infinity where $rot\,\overrightarrow{A} = \overrightarrow{H} = \overrightarrow{H}_0$. Combining the first terms Eq. (1.26) leads to

$$\int\left[\frac{i\hbar e}{m^*c}\left(\Psi^*\overrightarrow{\nabla}\Psi - \Psi\overrightarrow{\nabla}\Psi^*\right) + \frac{4e^2}{m^*c^2}\left|\Psi\right|^2\overrightarrow{A} + \frac{1}{4\pi}rot\,rot\,\overrightarrow{A}\right]\cdot\delta\overrightarrow{A}\,dV = 0\ . \qquad (1.28)$$

For arbitrary $\delta\overrightarrow{A}$, this can be zero only if the expression in the square brackets is zero:

$$\frac{i\hbar e}{m^*c}\left(\Psi^*\overrightarrow{\nabla}\Psi - \Psi\overrightarrow{\nabla}\Psi^*\right) + \frac{4e^2}{m^*c^2}\left|\Psi\right|^2\overrightarrow{A} + \frac{1}{4\pi}rot\,rot\,\overrightarrow{A} = 0\ . \qquad (1.29)$$

The current density $\vec{j}_S$ in the superconductor is given by the Maxwell equation

$$\vec{j}_S = \frac{c}{4\pi}rot\,rot\,\overrightarrow{A}\ , \qquad (1.30)$$

and, consequently, we obtain the second Ginzburg-Landau equation:

$$\vec{j}_S = -\frac{i\hbar e}{m^*}\left(\Psi^*\overrightarrow{\nabla}\Psi - \Psi\overrightarrow{\nabla}\Psi^*\right) - \frac{4e^2}{m^*c}\left|\Psi\right|^2\overrightarrow{A}\ . \qquad (1.31)$$

1.3.4 Characteristic length scales

The GL theory introduces two important characteristic length: the coherence length $\xi(T)$ and the penetration depth $\lambda(T)$.

Coherence length ξ. The coherence length $\xi(T)$ indicates the typical length scale over which the size of the order parameter can vary (Fig. 1.4). One can derive this length from the first Ginzburg-Landau equation (1.23) [18]. In this discussion we will limit ourselves to a semi-infinite superconductor with flat boundary at $x = 0$.

For a situation where no field is applied and for a gauge in which Ψ is real, Eq. (1.23) becomes in one dimension

$$\alpha\Psi + \beta\Psi^3 - \frac{\hbar^2}{2m^*}\frac{d^2}{dx^2}\Psi = 0 \ . \tag{1.32}$$

The nonzero solution describing the uniform superconducting state is given by

$$\Psi = \Psi_0 = \sqrt{-\frac{\alpha}{\beta}} \ . \tag{1.33}$$

Near the surface of the superconductor, for example, the value of $\Psi(x)$ is different from Ψ_0. To calculate the length scale over which the order parameter can vary, it is useful to write Ψ in dimensionless variables as

$$\Psi = f\Psi_0 \ . \tag{1.34}$$

Taking into account that $\alpha < 0$ Eq. (1.32) becomes

$$-\frac{\hbar^2}{2m^*\,|\alpha|}\frac{d^2 f}{dx^2} - f + f^3 = 0 \ , \tag{1.35}$$

which means that the charateristic length scale over which f (and thus Ψ) can change is given by

$$\xi(T) = \sqrt{\frac{\hbar^2}{2m^*\,|\alpha|}} \ . \tag{1.36}$$

Since α depends on the temperature as $\alpha \propto (T - T_{c0})$, the coherence length varies as a function of the temperature as

$$\xi(T) \propto (1 - T/T_{c0})^{-1/2} \ . \tag{1.37}$$

Notice that this is certainly not the same length as the BCS coherence length ξ_o Near T_c the relation between $\xi(T)$ and ξ_o depends on the purity of the material, defined by the elastic mean free path l_{el}:

$$\xi(T) = 0.74\xi_o\,(1 - T/T_{c0})^{-1/2} \ \text{ when } l_{el} \gg \xi_o \text{ (pure)}, \tag{1.38}$$

$$\xi(T) = 0.855\sqrt{\xi_o l_{el}}\,(1 - T/T_{c0})^{-1/2} \ \text{ when } l_{el} \ll \xi_o \text{ (dirty)}. \tag{1.39}$$

Notice further that the coherence length $\xi(T)$ diverges at the critical temperature T_{c0}.

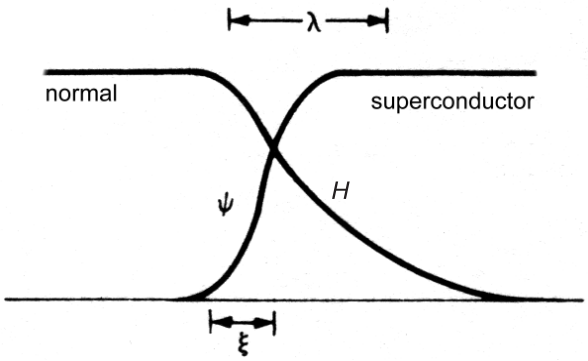

Fig. 1.4 The radial dependence of the order parameter Ψ and the magnetic field H at the superconducting/normal surface boundary. [from Ref. [25].]

Penetration depth λ. The typical length scale over which the magnetic field $\overrightarrow{H}$ can vary is the penetration depth $\lambda(T)$ (Fig. 1.4). This length scale can be derived in a similar way from the second Ginzburg-Landau equation (1.31) [18].

Let us consider the situation where $\Psi = \Psi_0$ and take the curl of both sides of Eq. (1.31):

$$rot\ \overrightarrow{j}_S = -\frac{4e^2}{m^* c} \left|\Psi\right|^2 rot\ \overrightarrow{A} \tag{1.40}$$

Using the Maxwell equation (1.30) we can rewrite this as

$$\overrightarrow{H} + \lambda^2 rot\, rot\, \overrightarrow{H} = 0\ , \tag{1.41}$$

and the charateristic length scale over which the magnetic field $\overrightarrow{H}$ can vary is given by

$$\lambda(T) = \sqrt{\frac{m^* c^2}{16\pi e^2 \left|\Psi_0\right|^2}} = \sqrt{\frac{m^* c^2}{8\pi e^2 n_s}} = \sqrt{\frac{m^* c^2 \beta}{16\pi \left|\alpha\right| e^2}}\ , \tag{1.42}$$

where the density of superconducting electrons $n_s = 2\left|\Psi_0\right|^2 = 2\left|\alpha\right|/\beta$ and the mass of a Cooper-pair is two times the electron mass m: $m^* = 2m$.

Also the penetration depth $\lambda(T)$ varies as a function of the temperature as

$$\lambda(T) \propto \left(1 - T/T_{c0}\right)^{-1/2}, \tag{1.43}$$

since $\left|\Psi_0\right|^2 \propto \left|\alpha\right| \propto (T_{c0} - T)$. The relation between the temperature dependent penetration depth $\lambda(T)$ and the London penetration depth $\lambda_L(0)$ at

absolute zero temperature differs for pure and dirty materials [25]:

$$\lambda(T) = \frac{\lambda_L(0)}{\sqrt{2}} \left(1 - T/T_{c0}\right)^{-1/2} \text{ when } l_{el} \gg \xi_o \text{ (pure)}, \tag{1.44}$$

$$\lambda(T) = \frac{\lambda_L(0)}{\sqrt{2}} \sqrt{\frac{\xi_o}{1.33 l_{el}}} \left(1 - T/T_{c0}\right)^{-1/2} \text{ when } l_{el} \ll \xi_o \text{ (dirty)}. \tag{1.45}$$

Notice that the penetration depth $\lambda(T)$ diverges at the critical temperature T_{c0}.

In this thesis, the Ginzburg-Landau equations are exploited within the dimensionless form. The distances will be expressed in units of the coherence length $\xi = \hbar/\sqrt{-2m^*\alpha}$, and the order parameter in $\Psi_0 = \sqrt{-\alpha/\beta}$ and the vector potential in $c\hbar/2e\xi$. $\kappa = \lambda/\xi$ is the Ginzburg-Landau parameter, and the penetration length is $\lambda = c\sqrt{m/\pi}/4e\Psi_0$. The magnetic field unit is the second critical magnetic field $H_{c2} = c\hbar/2e\xi^2 = \kappa\sqrt{2}H_c$, where $H_c = \sqrt{4\pi\alpha^2/\beta}$ is the critical field.

By exploiting these dimensionless variables and the London gauge, $div\,\overrightarrow{A} = 0$, Eqs.(1.23),(1.31) can be rewritten in the following form:

$$\left(-i\overrightarrow{\nabla} - \overrightarrow{A}\right)^2 \Psi = \Psi\left(1 - |\Psi|^2\right) \ , \tag{1.46}$$

$$-\kappa^2 \Delta \overrightarrow{A} = \frac{1}{2i}\left(\Psi^* \overrightarrow{\nabla}\Psi - \Psi\overrightarrow{\nabla}\Psi^*\right) - |\Psi|^2 \overrightarrow{A} \ , \tag{1.47}$$

with the boundary condition:

$$\overrightarrow{n} \cdot \left(-i\overrightarrow{\nabla} - \overrightarrow{A}\right)\Psi\Big|_{boundary} = 0 \ . \tag{1.48}$$

The temperature is included in ξ, λ, H_{c2}, through their temperature dependencies (see Eqs (1.37), (1.43) and $H_{c2} = c\hbar/2e\xi^2$)

$$\xi(T) = \frac{\xi(0)}{\sqrt{|1 - T/T_{c0}|}} \ , \tag{1.49}$$

$$\lambda(T) = \frac{\lambda(0)}{\sqrt{|1 - T/T_{c0}|}} \ , \tag{1.50}$$

$$H_{c2}(T) = H_{c2}(0)\left|1 - \frac{T}{T_{c0}}\right| \ , \tag{1.51}$$

where T_{c0} is the critical temperature at zero magnetic field.

1.3.5 Validity of the Ginzburg-Landau theory

Considering the validity of the Ginzburg-Landau equations, several points need to be discussed[19]:

1. Firstly, Landau assumes in his *theory of second order transitions* that the free energy can be expanded in powers of $|\Psi|^2$[7]. This is only valid near T_c where $|\psi|^2$ is small. Gor'kov showed theoretically that the Landau expansion is valid in the case of superconductors [21].

2. Ψ must be a *slowly varying function* over distances of the order of ξ_0. A necessary condition for the validity of the theory is, therefore, $\xi(T) \gg \xi_0$ or
$$\frac{T_{c0} - T}{T_{c0}} \ll 1, \tag{1.52}$$
i.e. temperature must be close to T_{c0}, the critical temperature in zero field.

3. The *local electrodynamic approximation* will be valid only if $\overrightarrow{H}$ and $\overrightarrow{A}$ are slowly varying functions over distances of the order of ξ_0. Therefore, it is necessary that $\lambda(T) \gg \xi_0$ or
$$\frac{T_{c0} - T}{T_{c0}} \ll \left[\frac{\lambda_L(0)}{\xi_0}\right]^2 , \tag{1.53}$$
which expresses again that temperature must be close to T_{c0}.

Although the Ginzburg-Landau theory has been derived only close to the superconducting/normal transition it turns out that its validity range is much larger. In particular, in mesoscopic superconductors the Ginzburg-Landau theory has been successfully used deep into the superconducting phase (see for example Ref. [20]).

1.4 TYPE-I AND TYPE-II SUPERCONDUCTORS

Superconductors can be separated into two types through their Ginzburg-Landau parameter $\kappa = \lambda(T)/\xi(T)$:

$$\kappa < 1/\sqrt{2} \rightarrow \text{ type-I superconductors,}$$
$$\kappa > 1/\sqrt{2} \rightarrow \text{ type-II superconductors.}$$

It is found that except niobium, all superconducting elements are type-I superconductors and Niobium and all superconducting alloys and chemical compounds are type-II. The new found high-T_c superconductors also belong to type-II superconductor.

For $\kappa < 0.42$ the material is a type-I superconductor. For fields below the thermodynamical critical field $\overrightarrow{H}_c$ the superconductor is in the Meissner state and all flux is expelled from the sample. At the critical field the magnetic field penetrates the sample, superconductivity is destroyed and the sample becomes normal. For $0.42 < \kappa < 1/\sqrt{2} \simeq 0.71$ the superconductor is still a

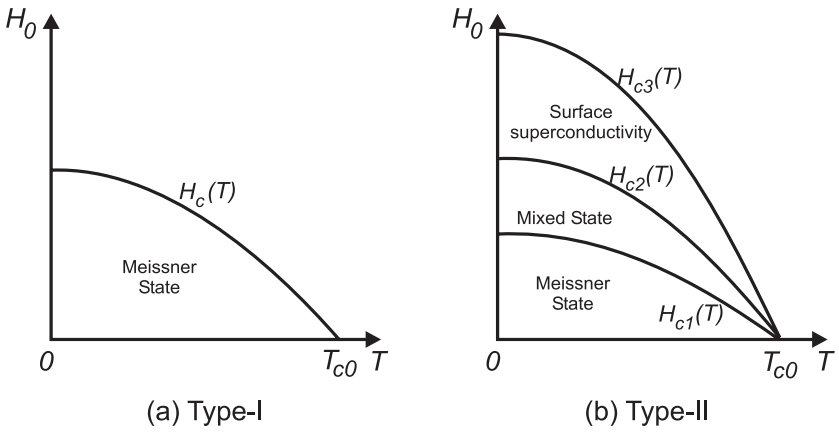

Fig. 1.5 $H-T$ phase diagram for a type-I (a) and a type-II (b) bulk superconductor.

type-I superconductor, but now the Meissner state does not jump immediately into the normal state with increasing field. At the field $\overrightarrow{H}_c$ flux can penetrate the inner part of the sample, while a layer remains superconducting near the surface of the sample. At the surface critical field $\overrightarrow{H}_{c3}$ the surface becomes normal too and the sample is in the normal state.

In type-II superconductors $\left(\kappa > 1/\sqrt{2}\right)$, on the other hand, a fourth possible state exists. In equilibrium, the Meissner state is only observed at applied fields $\overrightarrow{H}_0$ below the first critical field $\overrightarrow{H}_{c1}$. In the region between the first critical field $\overrightarrow{H}_{c1}$ and the second critical field $\overrightarrow{H}_{c2}$ the magnetic flux is able to penetrate the sample in quantized units of the flux quantum $\phi_0 = hc/2e$, called vortices. Abrikosov found that these vortices construct a triangular lattice inside the superconductor, the so-called Abrikosov vortex lattice. The state is called the Abrikosov vortex state or Mixed state. In the region $\overrightarrow{H}_{c2} < \overrightarrow{H}_0 < \overrightarrow{H}_{c3}$, superconductivity only exists at a thin layer near the sample edges, while the inner side of the sample is in the normal state. For bulk type-II superconductors the third critical field $\overrightarrow{H}_{c3}$ is approximately equal to $1.69\overrightarrow{H}_{c2}$. For larger fields superconductivity is destroyed and the entire sample is in the normal state.

The critical fields $\overrightarrow{H}_c$, $\overrightarrow{H}_{c1}$, $\overrightarrow{H}_{c2}$ and $\overrightarrow{H}_{c3}$ depend on the temperature. The $H-T$ phase diagram for type-I and type-II bulk superconductors are shown in Fig. 1.5.

Both types have also a different behavior of the magnetization as a function of the external magnetic field. This can be seen from Fig. 1.6.

Multivortex versus giant vortex state

Depending on the sample geometry, the size, the applied magnetic field and the temperature, different kinds of vortex states can nucleate in mesoscopic

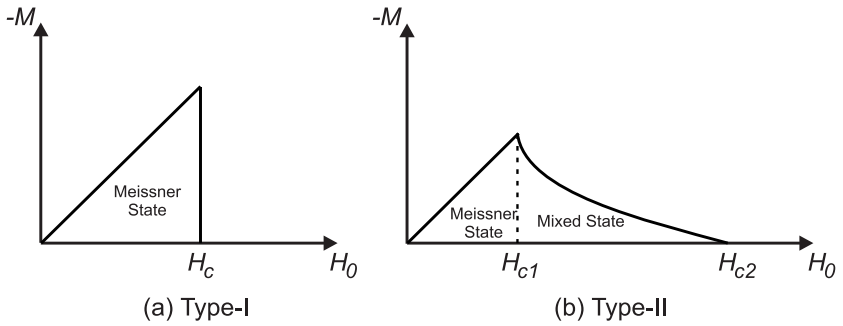

Fig. 1.6 The magnetization as a function of the applied magnetic field for type-I and type-II bulk superconductors.

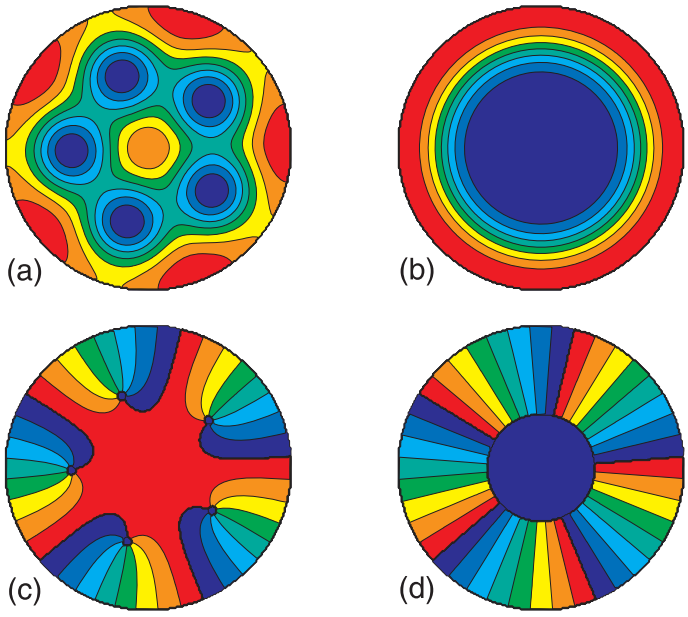

Fig. 1.7 The Cooper-pair density for the multivortex state (a) and the giant vortex state (b), and the phase of the order parameter for the multivortex state (c) and the giant vortex state (d) with vorticity $L = 5$ in a superconducting disk with radius $R/\xi = 6.0$. High (low) Cooper-pair density is given by red (blue) regions. Phases near 2π (0) are given by red (blue).

samples: giant vortex states and multi-vortex states, or a mixture of both of them.

The **multivortex** state in mesoscopic confined samples is the analogon of the Abrikosov vortex state in bulk superconductors. The flux penetrates the sample at several positions where vortices are created. These vortices can be

very close to each other and overlap, but they are defined by their separate zeros of the Cooper-pair density. On the other hand, when the sample is sufficiently small, the vortices will overlap so strongly that it is more favorable to form one big **giant vortex**, corresponding with only one minimum in the Cooper-pair density. The shape of the giant vortex also depends on the sample geometry. Figs. 1.7(a,b) show the Cooper-pair density for a multivortex state and a giant vortex state in a superconducting disk with radius $R/\xi = 6.0$. High Cooper-pair density is given by red regions, low by blue regions. This means that in Fig. 1.7(a) the blue spots are the vortices.

Vorticity

For a given mesoscopic sample, different superconducting states (giant vortex states and multivortex states) can nucleate for a particular magnetic field. These states have a different free energy and a different vortex configuration, and they can be characterized by their **vorticity** L. For multivortex states the vorticity is nothing else than the number of vortices. To determine the vorticity of the giant vortex state one has to look at the phase of the order parameter. Going around the center of the vortex, the phase of the order parameter changes always with L times 2π. Fig. 1.7(c) shows the contour plot of the phase of the order parameter for the multivortex state of Fig. 1.7(a). Blue indicate phases near zero and red phases near 2π. By going around near the boundary of the disk, the phase changes 5 times with 2π. This means that the total vorticity of the disk is $L = 5$. By going around one single vortex the phase changes with 2π and $L = 1$. In Fig. 1.7(d) the phase of the order parameter is shown for the giant vortex configuration of Fig. 1.7(b). By going around the giant vortex, the phase of the order parameter changes 5 times with 2π, which means that the giant vortex state has vorticity $L = 5$.

2

Theoretical formalism

We consider a mesoscopic superconducting sphere with radius R surrounded by vacuum. The externally applied magnetic field $\overrightarrow{H} = (0, 0, H)$ is uniform and directed in the z-direction. Since we neglect demagnetization effects, i.e. the bending of the magnetic field lines around the superconductor, we can restrict ourselves to the solution of the first Ginzburg-Landau equation. This approach is expected to be valid when $R \ll \lambda(T)$.

2.1 GIANT VORTEX STATES

As mentioned in the introduction, giant vortex states always have cylindrical symmetry in samples of circular symmetry. To find stable giant vortex states we first solve the linearized first Ginzburg-Landau equation. This is expected to be a good approximation near the S/N boundary when $|\psi|^2 \ll 1$ and correspondingly we may neglect the non-linear term in the GL equation. The linearized first GL equation can be written as follows in cylindrical coordinates:

$$\frac{1}{\rho}\frac{\partial}{\partial\rho}\left(\rho\frac{\partial\Psi}{\partial\rho}\right) + \frac{1}{\rho^2}\frac{\partial^2\Psi}{\partial\varphi^2} - 2is\frac{\partial\Psi}{\partial\varphi} - s^2\rho^2\Psi + \frac{\partial^2\Psi}{\partial z^2} = -\frac{2m}{\hbar^2}(-\alpha)\Psi, \qquad (2.1)$$

where

$$\begin{aligned} s &= \frac{eH}{\hbar c}, \\ H &= \frac{H}{H_{c2}}, \\ \rho &= \frac{\rho}{\xi}. \end{aligned} \tag{2.2}$$

Since

$$-\alpha(T) \equiv \frac{\hbar^2}{2m\xi^2}\left(1-\frac{T}{T_c}\right), \tag{2.3}$$

we can write

$$\frac{1}{\rho}\frac{\partial}{\partial\rho}\left(\rho\frac{\partial\Psi}{\partial\rho}\right)+\frac{1}{\rho^2}\frac{\partial^2\Psi}{\partial\varphi^2}-2is\frac{\partial\Psi}{\partial\varphi}-s^2\rho^2\Psi+\frac{\partial^2\Psi}{\partial z^2}=-\left(1-\frac{T}{T_c}\right)\Psi. \tag{2.4}$$

Giant vortex states are cylindrical symmetric and hence their order parameter should be cylindrical symmetric too, i.e.,

$$\Psi(\rho,\varphi,z)=e^{iL\varphi}\psi(\rho,z). \tag{2.5}$$

Therefore, Eq. 2.4 reduces to the following eigenvalue problem

$$-\frac{\partial^2\psi}{\partial\rho^2}-\frac{\partial^2\psi}{\partial z^2}-\frac{1}{\rho}\frac{\partial\psi}{\partial\rho}+\left(\frac{L^2}{\rho^2}+\frac{B^2\rho^2}{4}-BL\right)\psi=\varepsilon\psi, \tag{2.6}$$

where the eigenvalue $\varepsilon = 1-T/T_c$ and the order parameter ψ were found for fixed field and fixed disk radius by using the software package FEMLAB.

To follow the notation of Ref. [3] we use the $\widehat{L}$ operator, given by

$$\widehat{L}=-\frac{\partial^2}{\partial\rho^2}-\frac{\partial^2}{\partial z^2}-\frac{1}{\rho}\frac{\partial}{\partial\rho}+\left(\frac{L^2}{\rho^2}+\frac{B^2\rho^2}{4}-BL\right)-1, \tag{2.7}$$

and the eigenvalues and eigenfunctions of the $\widehat{L}$ operator can be found from the equation

$$\boxed{\widehat{L}\psi_{L,n}(\rho,z)=\Lambda_{L,n}\psi_{L,n}(\rho,z)}, \tag{2.8}$$

where $\Lambda=\varepsilon-1$ for fixed vorticity and radius, L is the vorticity and $n=1,2,...$ enumerates the different states for the same radius R and the same vorticity L.

The superconducting state starts to develop when the minimal eigenvalue of the operator $\widehat{L}$ is negative. The eigenvalue Λ also determines the minimal free energy F of the giant vortex states. For the giant vortex state we only consider the states which lie below the $F=0$ level. In this approximation the order parameter is given by

$$\Psi(\rho,\varphi,z)=\left(-\Lambda\frac{I_2}{I_1}\right)^{1/2}\psi_{L,n}(\rho,z)\exp(iL\varphi), \tag{2.9}$$

and the minimal free energy by

$$F = -\Lambda^2 \frac{I_2^2}{I_1}, \tag{2.10}$$

where

$$\begin{aligned} I_1 &= \int_{-R}^{R} dz \int_0^{\sqrt{R^2-z^2}} \rho d\rho \psi_{L,n}^4(\rho, z), \\ I_2 &= \int_{-R}^{R} dz \int_0^{\sqrt{R^2-z^2}} \rho d\rho \psi_{L,n}^2(\rho, z). \end{aligned} \tag{2.11}$$

2.2 MULTIVORTEX STATES

For sufficiently large spheres, and when we move away from the S/N boundary, the giant vortex state can break up into multivortices. In order to investigate such structures we use the method proposed by Schweigert *et al.* [5], Yampolskii *et al.* [3], and Palacios [1, 2] for disks, and extend it here to spheres in order to determine also the stability of the different multivortex configurations in spheres. Following Refs. [6] and [3] the order parameter of the multivortex state is written as a linear combination of the eigenfunctions of the linearized Ginzburg-Landau equation (2.1), i.e.

$$\Psi(\rho, \varphi, z) = \sum_{L=0}^{N} C_L \psi_L(\rho, z) exp(iL\varphi), \tag{2.12}$$

where the vorticity L is now the value of the effective total angular momentum which is equal to the number of vortices in the sphere. Notice that we restrict ourself to $n = 1$ as done in [1, 2, 3].

Substituting Eq. (2.12) in the free-energy expression (1.5) we obtain F as a function of the complex parameters $\{C_{L_j}\}$. Minimization of F with respect to these parameters allows us to find the equilibrium vortex configurations and to determine their stability. The extremal points are determined by the solutions $\{C_{L_j}^0\}$ of the set of equations

$$\frac{\partial F}{\partial C_{L_j}} = 0. \tag{2.13}$$

The stable vortex states are determined by the usual criterium for a multivariable function: the matrix of second derivative (also called the Hessian matrix), i.e.

$$\left. \frac{\partial^2 F}{\partial C_{L_j} \partial C_{L_k}} \right|_{C_{L_j}=C_{L_j}^0, C_{L_k}=C_{L_k}^0}, \tag{2.14}$$

must be positive definite. The giant vortices are also described by Eq. (2.12): they correspond to $C^0_{L_j} = 0$, except for one nonzero coefficient $C^0_{L_j=L}$. This allow us to check the stability of a giant vortex states with respect to transitions into a multivortex state.

Let us now consider states which are built up by only two components in Eq. (2.12). This restricts our analysis quantitatively but, nevertheless, will give the correct qualitative behavior and facilitates the physical insight into the problem. The free energy of a two-component state is

$$F = C^4_{L_1} A_{L_1} + C^4_{L_2} A_{L_2} + 4C^2_{L_1} C^2_{L_2} A_{L_1,L_2} + 2\Lambda_{L_1} C^2_{L_1} B_{L_1} + 2\Lambda_{L_2} C^2_{L_2} B_{L_2}, \tag{2.15}$$

where

$$\begin{aligned} A_{L_i} &= \int_{-R}^{R} dz \int_0^{\sqrt{R^2-z^2}} \rho d\rho \psi^4_{L_i}(\rho, z), \\ B_{L_i} &= \int_{-R}^{R} dz \int_0^{\sqrt{R^2-z^2}} \rho d\rho \psi^2_{L_i}(\rho, z), \\ A_{L_1,L_2} &= \int_{-R}^{R} dz \int_0^{\sqrt{R^2-z^2}} \rho d\rho \psi^2_{L_1}(\rho, z) \psi^2_{L_2}(\rho, z). \end{aligned} \tag{2.16}$$

Although, in general the C_{L_j} is a complex number, for our two-component state C_{L_j} are real numbers. Minimization of Eq. (2.15) with respect to C_{L_1} and C_{L_2} gives the possible equilibrium states:

(i) the normal state,

$$C^{(0)}_{L_1} = C^{(0)}_{L_2} = 0, \tag{2.17}$$

(ii) the giant vortex states,

$$\begin{aligned} C^{(0)}_{L_1} = 0, \qquad & C^{(0)}_{L_2} = \left(-\Lambda_{L_2} \frac{B_{L_2}}{A_{L_2}}\right)^{1/2}, \\ C^{(0)}_{L_1} = \left(-\Lambda_{L_1} \frac{B_{L_1}}{A_{L_1}}\right)^{1/2}, \qquad & C^{(0)}_{L_2} = 0, \end{aligned} \tag{2.18}$$

(iii) the multi vortex states

$$\begin{aligned} C^{(0)}_{L_1} &= \pm \left(\frac{-\Lambda_{L_1} A_{L_2} B_{L_1} + 2\Lambda_{L_2} A_{L_1,L_2} B_{L_2}}{A_{L_1} A_{L_2} - 4A^2_{L_{1,2}}} \right)^{1/2}, \\ C^{(0)}_{L_2} &= \pm \left(\frac{-\Lambda_{L_2} A_{L_1} B_{L_2} + 2\Lambda_{L_1} A_{L_1,L_2} B_{L_1}}{A_{L_1} A_{L_2} - 4A^2_{L_{1,2}}} \right)^{1/2}. \end{aligned} \tag{2.19}$$

To check the stability of the different vortex states, we have to calculate the components of the Hessian matrix (2.14), i.e.

$$\begin{aligned}
\frac{\partial^2 F}{\partial C_{L_1}^2} &= 12C_{L_1}^2 A_{L_1} + 8C_{L_2}^2 A_{L_1,L_2} + 4\Lambda_{L_1} B_{L_1}, \\
\frac{\partial^2 F}{\partial C_{L_2}^2} &= 12C_{L_2}^2 A_{L_2} + 8C_{L_1}^2 A_{L_1,L_2} + 4\Lambda_{L_2} B_{L_2}, \\
\frac{\partial^2 F}{\partial C_{L_1} \partial C_{L_2}} &= 16C_{L_1} C_{L_2} A_{L_1,L_2}, \qquad (2.20)
\end{aligned}$$

By substituting the solutions (2.17)-(2.19) into Eq. (2.15) we obtain the energies of the different equilibrium states and [from Eq. (2.20)] the corresponding conditions for their stability.

(i) For the **normal state**, we obtain $F = 0$. Notice from Eq. (2.20) that for negative $\Lambda_{L_1(L_2)}$ this state is always unstable.

(ii) The energies of the **giant vortex states** are

$$F_{L_i} = -\Lambda_{L_i}^2 \frac{B_{L_i}^2}{A_{L_i}^2}. \qquad (2.21)$$

Of course, they coincide with the F of Eq. (2.10). The conditions for stability are

$$\begin{aligned}
\frac{\partial^2 F}{\partial C_{L_1}^2} &= \frac{4}{A_{L_2}} (\Lambda_{L_1} A_{L_2} B_{L_1} - 2\Lambda_{L_2} A_{L_1,L_2} B_{L_2}) > 0, \\
\frac{\partial^2 F}{\partial C_{L_2}^2} &= -8\Lambda_{L_2} B_{L_2} > 0, \qquad (2.22)
\end{aligned}$$

and

$$\begin{aligned}
\frac{\partial^2 F}{\partial C_{L_2}^2} &= \frac{4}{A_{L_1}} (\Lambda_{L_2} A_{L_1} B_{L_2} - 2\Lambda_{L_1} A_{L_1,L_2} B_{L_1}) > 0, \\
\frac{\partial^2 F}{\partial C_{L_1}^2} &= -8\Lambda_{L_1} B_{L_1}, \qquad (2.23)
\end{aligned}$$

for the giant vortex states with vorticity L_1 and L_2 , respectively.

The superconducting current density has only an azimuthal component and is given by

$$j_{L_i}(\rho) = -\frac{\Lambda_{L_i} B_{L_i}}{A_{L_i}} \left(\frac{L_i}{\rho} - \frac{H\rho}{2} \right) \psi_{L_i}^2(\rho). \qquad (2.24)$$

(iii) The energy of the **multivortex state** becomes

$$F_{L_1,L_2} = \frac{-\Lambda_{L_1}^2 A_{L_2} B_{L_1}^2 - \Lambda_{L_2}^2 A_{L_1} B_{L_2}^2 + 4\Lambda_{L_1}\Lambda_{L_2} A_{L_1,L_2} B_{L_1} B_{L_2}}{A_{L_1} A_{L_2} - 4A_{L_1,L_2}^2}, \tag{2.25}$$

and the corresponding stability conditions are

$$\begin{aligned} \frac{\partial^2 F}{\partial C_{L_1}^2} &= 8A_{L_1} \frac{-\Lambda_{L_1} A_{L_2} B_{L_1} + 2\Lambda_{L_2} A_{L_1,L_2} B_{L_2}}{A_{L_1} A_{L_2} - 4A_{L_1,L_2}^2} > 0, \\ \frac{\partial^2 F}{\partial C_{L_2}^2} &= 8A_{L_2} \frac{-\Lambda_{L_2} A_{L_1} B_{L_2} + 2\Lambda_{L_1} A_{L_1,L_2} B_{L_1}}{A_{L_1} A_{L_2} - 4A_{L_1,L_2}^2} > 0, \end{aligned} \tag{2.26}$$

and

$$\begin{aligned} \frac{\partial^2 F}{\partial C_{L_1}^2}\frac{\partial^2 F}{\partial C_{L_2}^2} - \left(\frac{\partial^2 F}{\partial C_{L_1}\partial C_{L_2}}\right)^2 &= (-\Lambda_{L_1} A_{L_2} B_{L_1} + 2\Lambda_{L_2} A_{L_1,L_2} B_{L_2}) \\ &\times (-\Lambda_{L_2} A_{L_1} B_{L_2} + 2\Lambda_{L_1} A_{L_1,L_2} B_{L_1}) \\ &\times \frac{64}{A_{L_1} A_{L_2} - 4A_{L_1,L_2}^2} > 0. \end{aligned} \tag{2.27}$$

The superconducting current density in the multivortex state is

$$\begin{aligned} & j_{L_1,L_2}(\rho,\varphi,z) = \\ & (C_{L_1}^{(0)})^2 \psi_{L_1}^2(\rho,z)\left(\frac{L_1}{\rho} - \frac{H\rho}{2}\right) + (C_{L_2}^{(0)})^2 \psi_{L_2}^2(\rho,z)\left(\frac{L_2}{\rho} - \frac{H\rho}{2}\right) \\ + \quad & (C_{L_1}^{(0)})(C_{L_2}^{(0)})\psi_{L_1}(\rho,z)\psi_{L_2}(\rho,z)\left(\frac{L_1+L_2}{\rho} - \frac{H\rho}{2}\right)\cos(L_2 - L_1)\varphi. \end{aligned}$$

3

Giant vortex states

First we study numerically the giant vortex states in superconducting spheres with radius $R = 2.0$, 4.0 and 6.0ξ. To study these axially symmetric states we use the theoretical formalism as described in section 2.1. The solutions of the linearized Ginzburg-Landau equation, including the eigenvalues and the order parameter are obtained by using the software packages MATLAB and FEMLAB.

3.1 ORDER PARAMETER, COOPER-PAIR DENSITY, PHASE

For a given vorticity and a given applied magnetic field, we obtain the Cooper-pair density in the $\rho - z$ plane, by using FEMLAB. By interpolation, using MATLAB, we can calculate the Cooper-pair density in the xy-plane. Next, we calculate the phase of the order parameter in the xy-plane.

First, we show in Fig. 3.1, as an example, contour plots of the Cooper-pair density for a sphere with radius $R = 4\xi$, for vorticity $L = 0, 1, 2$, and 3 at applied magnetic fields $H = 0.18H_{c2}$ and $H = 0.42H_{c2}$. High Cooper-pair density is given by red regions, while low Cooper-pair density is given by blue regions.

For $L = 0$, no vortex is present and the Cooper-pair density is highest around the z-axis. Notice that the highest density is focused around the poles of the sphere. For higher L, magnetic field penetrates the sphere and a giant vortex is formed around the z-axis, which leads to $|\Psi|^2 = 0$ for $\rho = 0$ for all values of z. Now the highest density of cooper-pair is found around

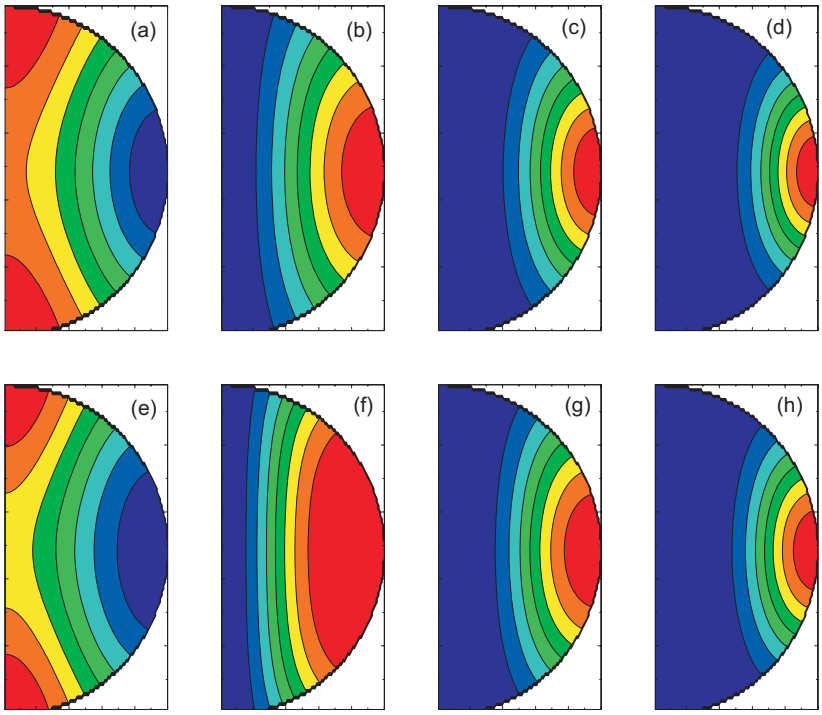

Fig. 3.1 Contour plots of the Cooper-pair density for a sphere with radius $R = 4\xi$ for vorticity $L = 0$ (a,e), $L = 1$ (b,f), $L = 2$ (c,g), and $L = 3$ (d,h) at applied magnetic fields $H = 0.18H_{c2}$ (a-d) and $0.42H_{c2}$ (e-h). The vertical axis corresponds to the direction of the applied magnetic field, i.e. the z-direction, while the horizontal axis corresponds to the radial direction ρ. High Cooper-pair density is given by red regions, while low Cooper-pair density is given by blue regions.

the equator. With increasing vorticity, the radius of the giant vortex states increases, just like in the case of thin disks (see Ref. [5]). With increasing field, the cooper-pair density in the meissner state is more suppressed while for larger vorticity the opposite behavior is forced.

Next, we calculate the Cooper-pair density in the xy-plane at $z = 0$ for the same parameters as in Figs. 3.1(a-d). Contour plots of these results are given in Figs. 3.2(a-d). These results are very similar to the results of thin disks with radius R. For $L = 0$ the Cooper-pair density is highest in the center, while it decreases with increasing ρ. When $L > 0$ Cooper-pair density is zero in the center, where the giant vortex is situated. Notice that from Figs. 3.2(a-c) it is clear that the size of the giant vortex in the center of the sphere increases with increasing L.

In Fig. 3.3 we show the Cooper-pair density in the xy-plane in a different way, by plotting the ρ dependence of $|\Psi|^2$ for $z = 0$ for $L = 0 - 8$ at

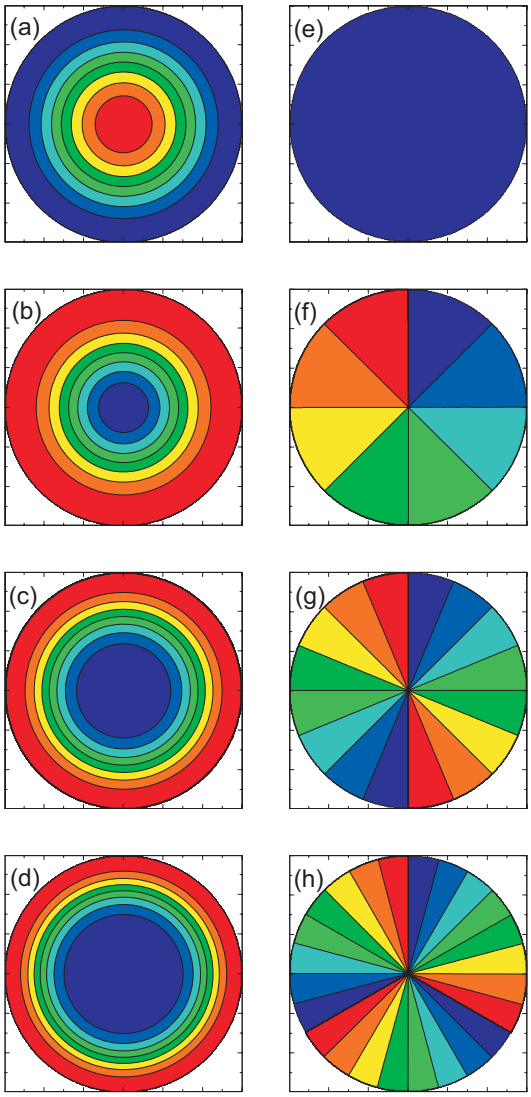

Fig. 3.2 (a-d) Contour plots of the Cooper-pair density in the xy-plane, i.e. $z = 0$, for a sphere with radius $R = 4\xi$ for vorticity $L = 0, 1, 2, 3$ at $H = 0.18H_{c2}$. High (low) Cooper-pair density is given by red (blue). (e-h) Phase of the order parameter for the same parameters as in (a-d). Red (blue) indicates phases near 2π (0).

$H = 0.18H_{c2}$. It should be noticed that, since we solve the linear equation, the absolute values of $|\Psi|^2$ has no meaning, but we find a qualitative radial dependence of $|\Psi|^2$ for vorticity L. If we want to have the correctly scaled values for $|\Psi|^2$, we should use Eq. (2.9). For $L = 0$ we find that the Cooper-pair

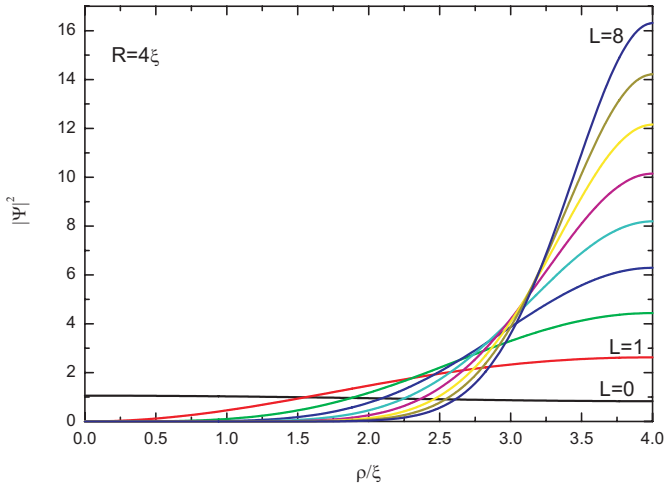

Fig. 3.3 ρ dependence of the Cooper-pair density $|\Psi|^2$ for $z = 0$ for $L = 0 - 8$ at $H = 0.18H_{c2}$.

density is highest in the center of the sphere, while it decreases with increasing ρ. For $L > 0$ we find zero Cooper-pair density exactly at $\rho = 0$, and a region of low Cooper-pair density around this region. From Fig. 3.3 it is clear that the size of this region increases with increasing L, which corresponds to an increasing size of the giant vortex in the center when the vorticity increases.

The order parameter of the giant vortex state is given by Eq. (2.5), i.e.,

$$\Psi(\rho, \varphi, z) = |\psi(\rho, z)|e^{iL\varphi}. \tag{3.1}$$

The size of the order parameter, $|\psi(\rho, z)|$, can be seen from Figs. 3.2(a-d). In Figs. 3.2(e-h), the phase of the order parameter in the xy plane at $z = 0$ is shown for the giant vortex states with vorticity $L = 0, 1, 2$, and 3, corresponding to the situations of Figs. 3.2(a-d). In these figures, red indicates phases near 2π and blue phases near zero. By going around the center of the vortex, the phase jumps L times with 2π. This property also shows that we just have to look at the phase of the order parameter to determine the vorticity of the giant vortex state.

3.2 EIGENVALUES

When solving the eigenvalue equation (2.8) using FEMLAB we obtain the eigenvalues Λ as a function of the applied magnetic field H for fixed radius R for all L. Figs. 3.4(a-c) show the eigenvalue as a function of the applied magnetic field for spheres with radius $R = 2$, 4, and 6ξ, respectively. For

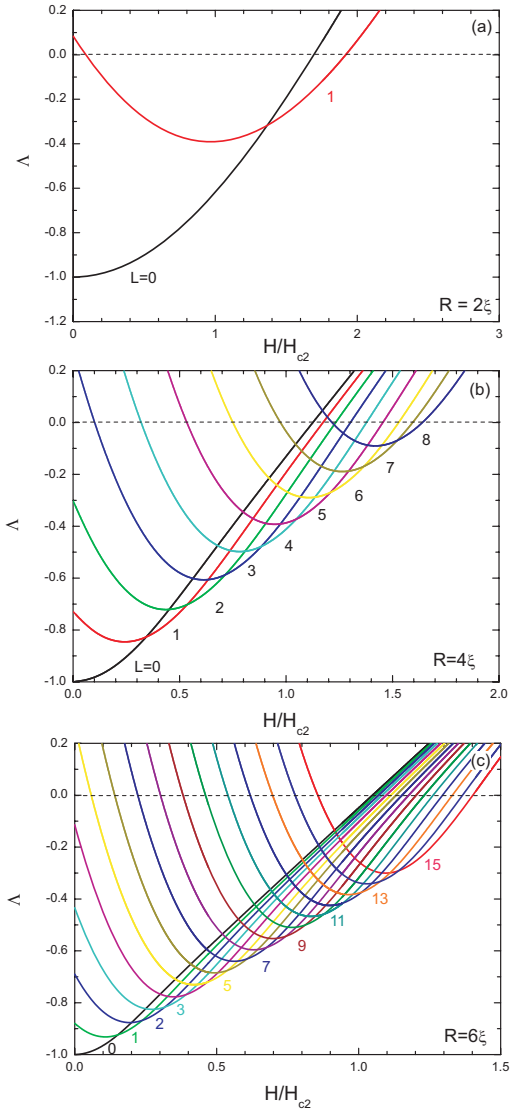

Fig. 3.4 The eigenvalue Λ as a function of the applied magnetic field H for spheres with radius $R = 2$ (a), 4 (b), and 6ξ (c).

$R = 2$ and 4ξ we show all stable states, i.e. states with $\lambda < 0$ in a certain magnetic field region. Notice that the dashed horizontal line corresponds to the $\Lambda = 0$ level. For $R = 6\xi$ we restrict ourselves to states with $L \leq 15$.

From Figs. 3.4(a-c) it is clear that with increasing sphere radius, more vortex states stabilizes, i.e. more vortex states corresponds to eigenvalues

with $\lambda < 0$. The ground state transitions between the different vortex states move to lower fields with increasing sphere radius, just like the superconducting/normal transition field. Notice that this behavior is qualitatively very similar to the behavior of the eigenvalues for a superconducting disk, which are shown in Ref. [3].

3.3 FREE ENERGY

From the order parameter and the eigenvalues we can calculate the free energy F as a function of the applied magnetic field for the different values of L using equations (2.10)-(2.11), i.e.,

$$F = -\Lambda^2 \frac{I_2^2}{I_1}, \tag{3.2}$$

where

$$\begin{aligned} I_1 &= \int_{-R}^{R} dz \int_0^{\sqrt{R^2-z^2}} \rho d\rho \psi_{L,n}^4(\rho, z), \\ I_2 &= \int_{-R}^{R} dz \int_0^{\sqrt{R^2-z^2}} \rho d\rho \psi_{L,n}^2(\rho, z). \end{aligned} \tag{3.3}$$

The dependence of the free energy F on the magnetic field H is shown in Figs. 3.5(a-c) for all the possible stable vortex states for spheres with radius $R = 2$, 4, and 6ξ, respectively. The free energy is in the unit of F_0. The dashed horizontal line corresponds to the zero energy level. Through the comparison of the magnetic dependence of the free energy for three different sphere radii, we can clearly find that with increasing radius R, the number of vortex states with negative free energy increase. From Figs. 3.5(a-c) it is also clear that with increasing radius R, the critical magnetic field, where F becomes zero, decreases.

Looking at the free energy curves, we see that for a certain magnetic field different vortex states can exist. The state with the lowest free energy is called the *ground state*, while the other states are the *meta-stable states*. The ground state corresponds to a global minimum, while the meta-stable states correspond to a local minimum in the free energy. The envelope of the lowest state curves in each of the figure represents the field dependence of the ground states. When following the ground state with increasing field, the vortex state will jump from $L \to L + 1$ at the field where the energy curves of the two vortex states cross each other. For example, the $L = 0 \to L = 1$ transition for the radius of $R = 4\xi$ occurs at the magnetic $H = 0.345 H_{c2}$. We can also find that these crossing points shift toward lower field with increasing radius R.

Notice that all free energy curve end exactly at $F = 0$ when increasing or decreasing the field. This doesn't mean that those vortex states are really

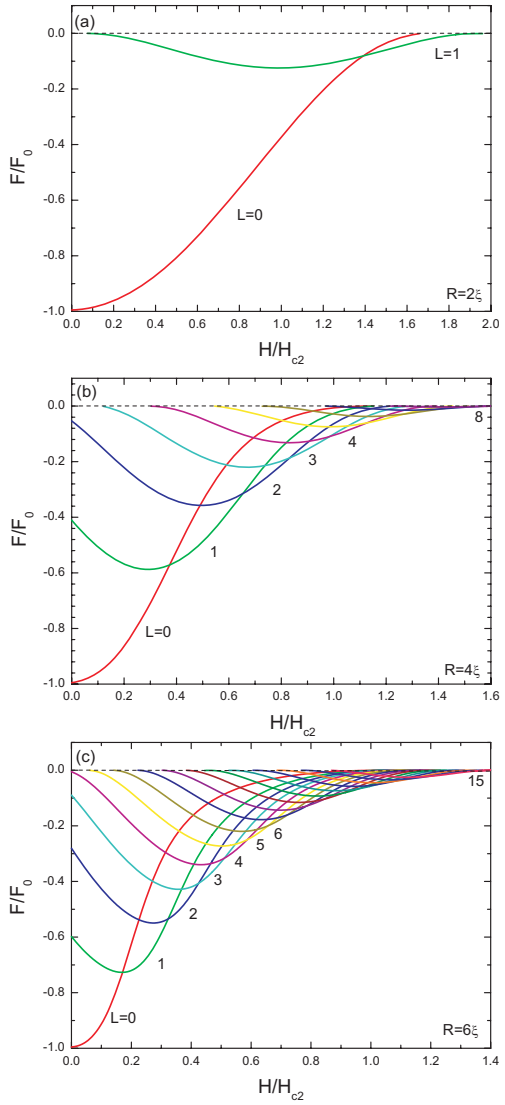

Fig. 3.5 The free energy F as a function of the applied magnetic field H for the giant vortex states in a sphere with radius $R = 2$ (a), 4 (b), and 6ξ (c).

(meta-)stable over this whole region, as we will show later when considering linear combinations of different giant vortex states.

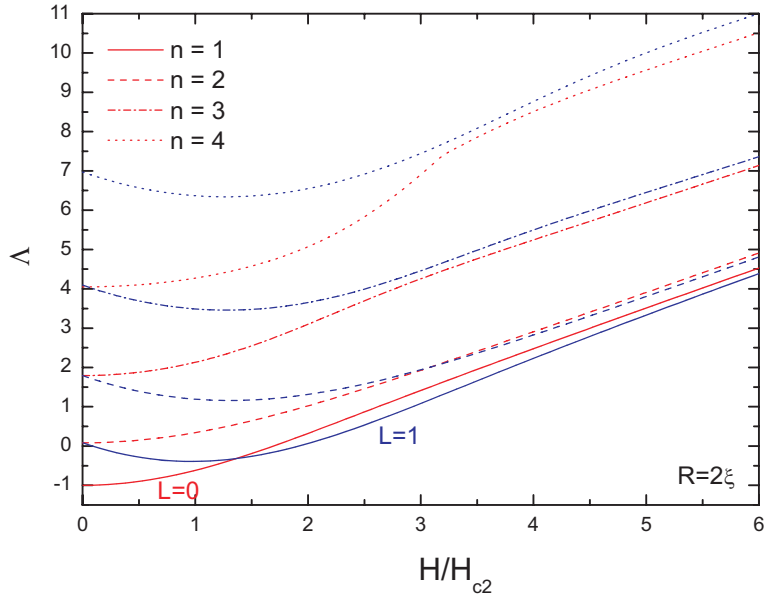

Fig. 3.6 The eigenvalue Λ as a function of the applied magnetic field for the states with $L = 0$ (red curves) and $L = 1$ (blue curves) corresponding to the lowest eigenvalue (solid curves), the first excited state (dashed curves), the second excited state (dash-dotted curve) and the third excited state (dotted curve).

3.4 EXCITED STATES

Up to now, we only focused on the properties of non-excited states for the possible angular momenta, which means the states corresponding to the lowest eigenvalue for a certain magnetic field, sphere radius and vorticity. Now, we will investigate the field of excited states.

In Fig. 3.6, the magnetic dependence of the eigenvalue Λ for both the excited and non-excited states with vorticity $L = 0$ and $L = 1$ are given for a sphere with radius $R = 2\xi$. The red curves correspond to $L = 0$ and the blue curves are for vorticity $L = 1$. The solid curve is for the non-excited state. The dashed, dash-dotted, and the dotted curves correspond to the first, second and the third excited states. Since all the excited states have positive eigenvalues for all magnetic fields, it is clear that they are not stable. Later, this will have the consequence that we do not have to take into account the excited states when we combine these giant vortex states in Eq. (2.12) to create multivortex states.

Although the excited states are not stable, we show, as an example, in Figs. 3.7(a-f) contour plots of the Cooper-pair density of the first ($n = 2$), second ($n = 3$) and third ($n = 4$) excited states for $L = 0$ (Figs. 3.7(a-c)) and

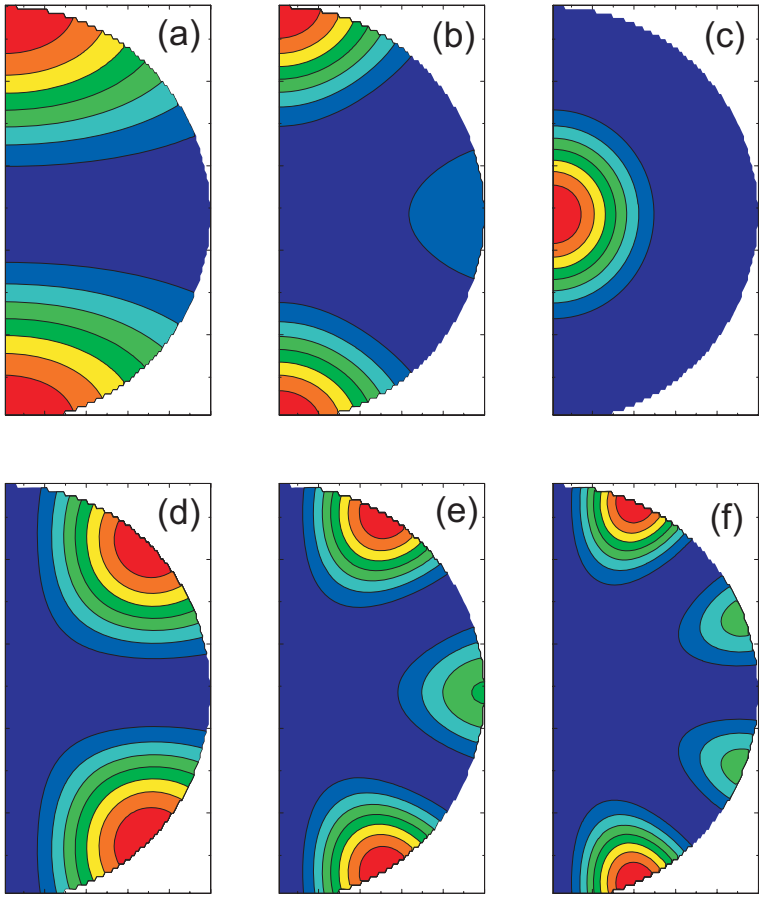

Fig. 3.7 Contour plots of the Cooper-pair density of the first ($n = 2$), second ($n = 3$) and third ($n = 4$) excited states for $L = 0$ (a-c) and $L = 1$ (d-f) at $H = 0.6H_{c2}$. High (low) Cooper-pair density is given by red (blue) regions.

$L = 1$ (Figs. 3.7(d-f)) at $H = 0.6H_{c2}$. High Cooper-pair density is given by red regions, while low Cooper-pair density is given by blue regions. For $n = 2$ we find two maxima in the Cooper-pair density around the sphere poles, both for $L = 0$ and $L = 1$. For $n = 3$ we find three maxima in both cases. For $n = 4$ we find 4 maxima near the sphere boundary for $L = 1$, but only one maximum for $L = 0$ that is located near the sphere center.

4
Multivortex states

When the radius of the sphere becomes large enough it is sometimes energetically more favorable for the giant vortex to split into single vortices which are separated from each other. This state is called the *multivortex state*. Contrary to the situation of the thin disks of Ref. [3], where the vortices were straight lines in the direction of the applied magnetic field, we can expect a different behavior in spheres. Now, it can be expected that the vortices bend towards the sphere boundary when approaching the top or bottom of the sphere.

To calculate the different (meta-)stable multivortex states in spheres, we use the formalism that we described in section 2.2, where we take linear combinations of two giant vortex state to construct a multivortex state.

As a notation we will use L-state for the giant vortex state with vorticity L, while for the multivortex state which is constructed as linear combination of the giant vortex state with vorticity L_1 and the giant vortex state with vorticity L_2, we will write (L_1, L_2)-state.

4.1 FREE ENERGY

First, we calculate the free energy of all the meta-stable states in a superconducting sphere with radius $R = 2$, 4 and 6ξ as a function of the applied magnetic field. This gives us the possibility to check the dependence of the stability of the multivortex state on the sphere size. Fig. 4.1 shows the free energy for the sphere with $R = 2\xi$. Since the radius of the sphere is so small, only the 0-state and the 1-state stabilize, as we could also conclude from

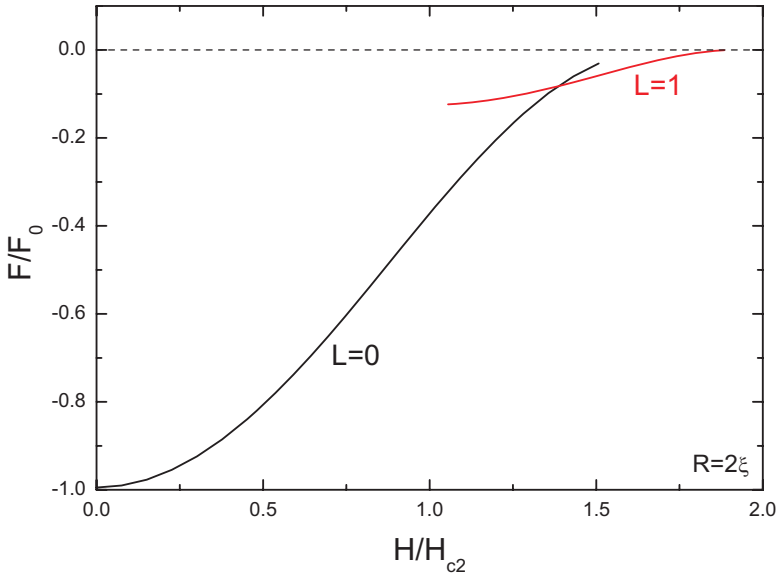

Fig. 4.1 The Free energy as a function of the applied magnetic field for the (meta-) stable states in a superconducting sphere with radius $R = 2\xi$.

Fig. 3.5(a). The free energy of the $L = 0$ and the $L = 1$-state as a function of the magnetic field is exactly the same as in Fig. 3.5(a), but the stability region decreases. To calculate the stability of the different giant vortex states we use equation (2.22).

When we increase the sphere size, more multivortex states become stable over a certain magnetic field region. In Fig. 4.2 we show the free energy of all (meta-)stable giant and multivortex states in a sphere with radius $R = 4\xi$ as a function of the applied magnetic field. The high magnetic field region is given in more detail in Fig. 4.2(b). Giant vortex states are given by solid curves, $(0, L)$ multivortex states by dashed curves, $(1, L)$ multivortex states by dotted curves and $(L > 1, L)$ multivortex states by dash-dotted curves. We find that giant vortex states stabilize for $L = 0$ up to $L = 8$, $(0, L)$-states for $L = 2 - 7$, $(1, L)$-states for $L = 4 - 7$, and also the $(2, 7)$ and the $(3, 8)$-states stabilize. It is clear that for fixed total vorticity L, several vortex states can nucleate at a certain magnetic field. As an example, for $L = 6$, we find that at $H_0/H_{c2} = 0.95$ two multivortex states are meta-stable, i.e. the $(0, 6)$-state and the $(1, 6)$-state. When we compare the free energy of these states we clearly see that the $(1, 6)$-state has lower energy than the $(0, 6)$-state. Just like in the case for disks we find continuous transitions between giant vortex states with vorticity L and the $(0, L)$-states when increasing or decreasing the applied

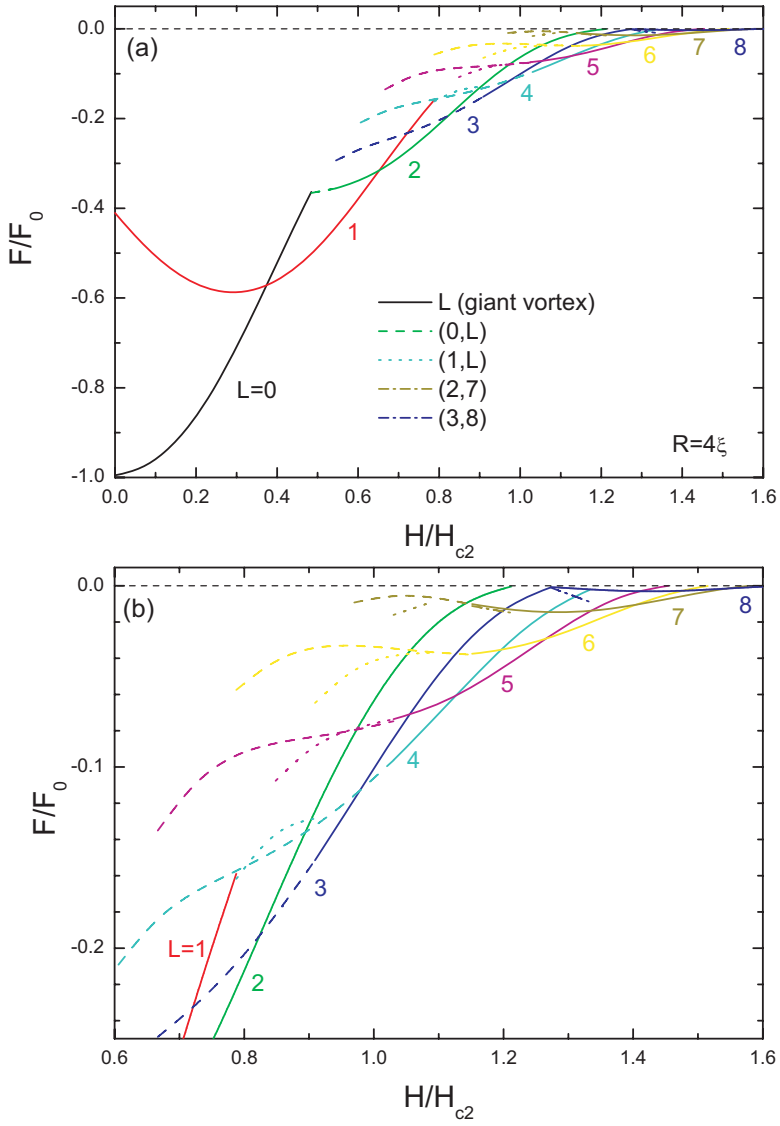

Fig. 4.2 (a) The Free energy as a function of the applied magnetic field for all the (meta-)stable states in a superconducting sphere with radius $R = 4\xi$. (b) The high magnetic field region in more detail.

magnetic field. There is no jump in the free energy at these transitions. All other transitions occur by jumps and are of first order.

Next, we study the ground state, i.e. the state with lowest free energy, as a function of the applied magnetic field. At low fields the Meissner state with

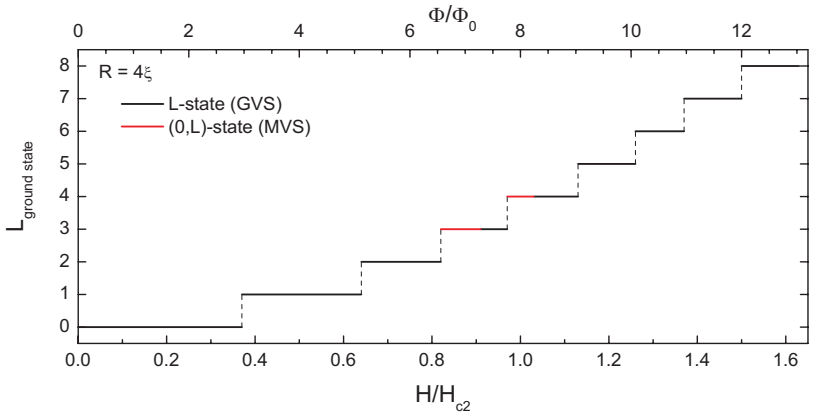

Fig. 4.3 Vorticity of the ground state for a sphere with radius $R = 4\xi$ as a function of the applied magnetic field. Giant vortex states are shown by black, $(0, L)$-states by red. The vertical lines indicate the transition fields. The top axis gives the flux penetrating the equator

$L = 0$ is the ground state. Around $H/H_{c2} = 0.37$ the free energy of the 0-state equals the one of the 1-state. When we further increase the magnetic field, the 1-state becomes the ground state up to $H/H_{c2} = 0.64$ when the 2-state becomes the ground state, etc. Notice that for $L = 3$ and 4, the ground state is first given by the $(0, L)$-state and then by the giant vortex state. To show the variation of the ground state as a function of the applied magnetic field we plot in Fig. 4.3 the vorticity of the ground state as a function of the field. When the ground state is a giant vortex state, the result is given by black curves. When the ground state is the $(0, L)$-state, the result is given by red curves.

When we further increase the sphere radius to $R = 6\xi$, much more linear combinations lead to (meta-)stable multivortex states. Considering only the states with total vorticity $L \leq 15$, we find 89 states which are (meta-)stable over a certain magnetic field region. Giant vortex states nucleate for all values of the vorticity from $L = 0$ up to $L = 15$, the $(0, L)$-state for $L = 2 - 15$, the $(1, L)$ for $L = 4 - 15$, the $(2, L)$ for $L = 5 - 15$, the $(3, L)$ for $L = 7 - 15$, the $(4, L)$ for $L = 8 - 15$, the $(5, L)$ for $L = 10 - 15$, the $(6, L)$ for $L = 11 - 15$, the $(7, L)$ for $L = 12 - 15$, the $(8, L)$ for $L = 14, 15$, and finally also the $(9, 15)$-state nucleates.

Fig. 4.4 shows the vorticity of the ground state as a function of the applied magnetic field. The different types of curves correspond to the different kind of states. The ground state is a giant vortex state for $L \leq 2$ and $L \geq 13$, a $(0, L)$-state for $L = 3 - 5$, a $(1, L)$-state for $L = 6 - 8$, a $(2, L)$-state for $L = 10$ over the whole magnetic field region where the state with vorticity L is a ground state. For $L = 9, 11, 12$ we find a transition between two

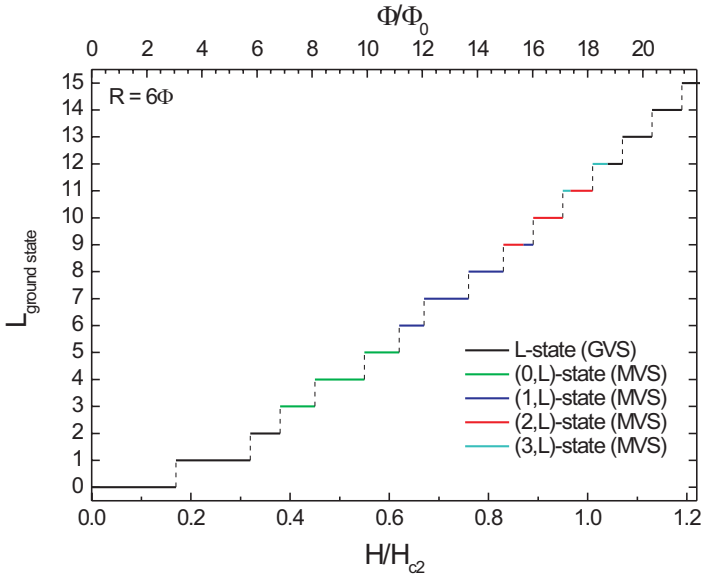

Fig. 4.4 Vorticity of the ground state for a sphere with radius $R = 6\xi$ as a function of the applied magnetic field.

different vortex states. For $L = 9$ the ground state is first the $(2, 9)$-state and transits with increasing field to the $(1, 9)$-state. Notice that this transition is of first order. For $L = 11$ the $(3, 11)$-state transits into the $(2, 11)$-state with increasing field, while for $L = 12$ the $(3, 12)$-state transits into the giant vortex state with $L = 12$.

4.2 COOPER-PAIR DENSITY FOR $Z = 0$

Now we will study the Cooper-pair density in the xy-plane of the sphere. In Fig. 4.5 contour plots of the Cooper-pair density in the xy plane are shown for a sphere with radius $R = 4\xi$. Figs. 4.5(a-d) correspond to the $(0 : 3), (0 : 4), (0 : 5), (0 : 6)$-states at a magnetic field $H = 0.85H_{c2}$. High Cooper-pair density is given by red regions, blue Cooper-pair density by blue regions. The white point is the center of the vortex where the Cooper-pair density $|\Psi|^2 < 0.001$. When we combine a giant vortex state with $L = 0$ with a giant vortex state with $L = L_1 > 0$, we find that the vortex state consists of L_1 vortices located on a shell, while there is no vortex in the center.

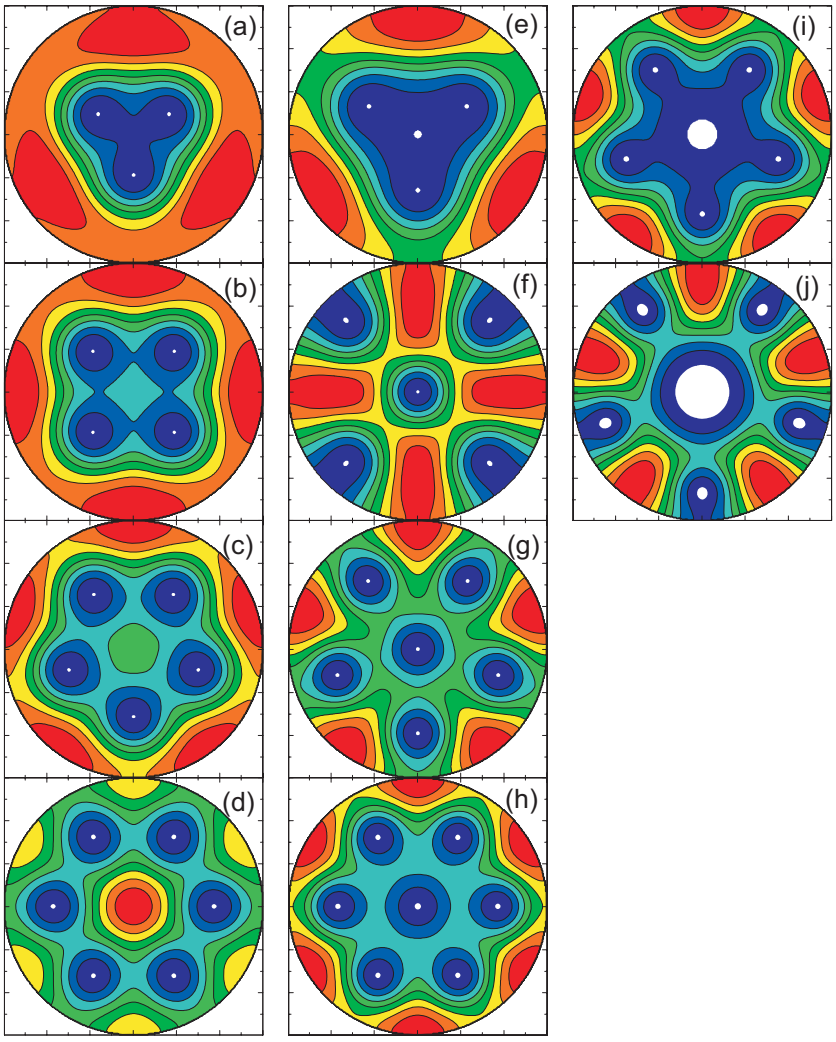

Fig. 4.5 Contour plots of the Cooper-pair density in the xy-plane of a sphere with radius $R = 4\xi$ for the $(0:3), (0:4), (0:5), (0:6)$-states at $H = 0.85H_{c2}$ (a-d), the $(1,4), (1,5), (1,6), (1,7)$-states at $H/H_{c2} = 0.38, 0.42, 0.79, 0.87$ (e-h), and the $(2,7)$-state and the $(3,8)$-state at $H = 1.1H_{c2}$ (i,j). High (low) Cooper-pair density is given by red (blue).

What happens when we take a linear combination of two giant vortex states with $L > 0$. Let us first consider the $(1, L_1)$-states, i.e. the linear combination of the $L = 1$ giant vortex state and a giant vortex state with vorticity L_1. In Figs. 4.5(e-h), the Cooper-pair density in the xy-plane for the $(1,4)$, the $(1,5)$, the $(1,6)$, and the $(1,7)$-state in a sphere with radius $R = 4\xi$ are shown

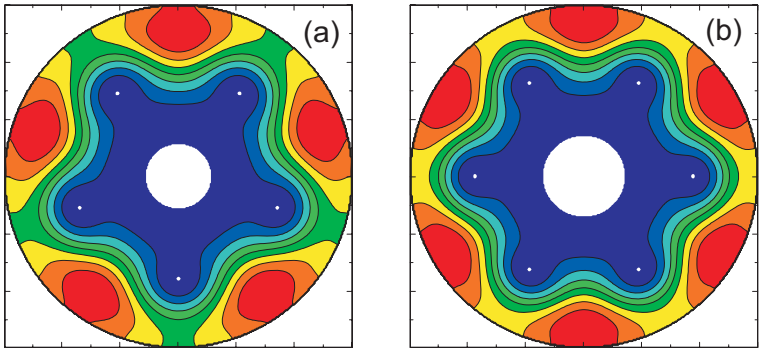

Fig. 4.6 Contour plots of the Cooper-pair density in the xy-plane of a sphere with radius $R = 6\xi$ for the $(4, 9)$ and $(5, 11)$-state.

at $H/H_{c2} = 0.38, 0.42, 0.79, 0.87$, respectively. From Fig. 4.2 we know that the magnetic field ranges over which these $(1, L_1)$-states are stable are much smaller than in the case for the $(0, L_1)$-states. The $(1, L_1)$-states only exist only in very narrow magnetic field regions. From Figs. 4.5(e-h) we can see that now there is one vortex in the center while $L_1 - 1$ vortices are situated on a shell around this central vortex.

Next, we try to find stable linear combinations of two giant vortex states with $L > 1$ for $R = 4\xi$. We find that only two of these states are stable, i.e. the $(2, 7)$-state and the $(3, 8)$-state. The Cooper-pair density of these multivortex states are shown in Figs. 4.5(i,j) at $H = 1.1H_{c2}$. In both cases the multivortex state consists of a giant vortex in the center with several single vortices on a shell around this central giant vortex. For the $(2, 7)$-state we find a giant vortex with vorticity $L = 2$ in the center, while for the $(3, 8)$-state the central giant vortex has vorticity $L = 3$. In both cases the giant vortex is encircled by a shell of 5 single vortices.

With increasing sphere radius the (L_1, L_2)-multivortex stabilizes for much more values of L_1 and L_2. For spheres with radius $R = 6\xi$ we find that multivortex states up to the combination of $L_1 = 9$ and $L_2 = 15$ can be stabilized. As an example, we show contour plots of the $(4, 9)$-state and $(5, 11)$-state in a sphere with radius $R = 6\xi$ in Figs. 4.6(a,b). The $(4, 9)$-state consists of a central giant vortex with vorticity $L = 4$, encircled by 5 single vortices, and the $(5, 11)$-state consists of a giant vortex with vorticity 5 in the center and 6 single vortices on a shell around this vortex.

Up to now, we gave examples of stable multivortex states at a certain magnetic field. But what is the influence of the magnetic field on the position of the vortices? To show the effect of the magnetic field we plot in Figs. 4.7(a-d) the $(0, 4)$-state in a sphere with radius $R = 4\xi$ at several values of the applied magnetic field, i.e. $H = 0.61H_{c2}$, $H = 0.73H_{c2}$, $H = 0.85H_{c2}$, and $H = 1.03H_{c2}$, respectively. With increasing magnetic field, the vortices clearly

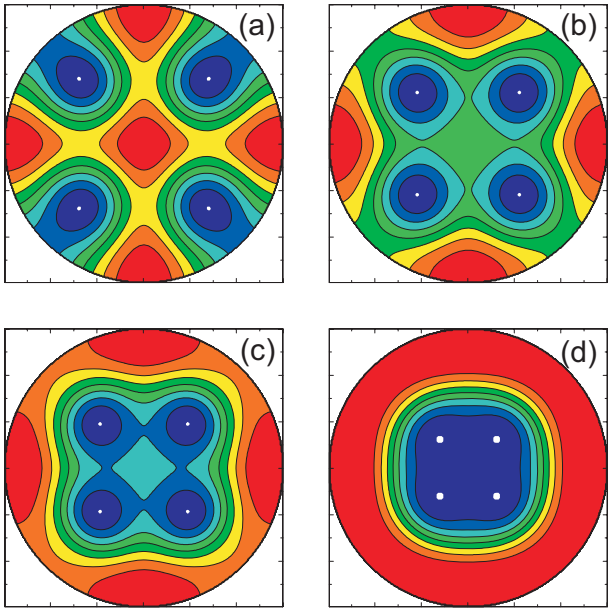

Fig. 4.7 Contour plots of the Cooper-pair density in the xy-plane of a sphere with radius $R = 4\xi$ for the $(0, 4)$-state at $H/H_{c2} = 0.61, 0.73, 0.85, 1.03$.

move in the direction of the center. Notice that in Fig. 4.7(d) the vortices of the $(0, 4)$-state are very close to the center. When we further increase the applied magnetic field, the 4 vortices recombine in the center into one big giant vortex with vorticity $L = 4$, which means that the $(0, 4)$ multivortex state transits into a $L = 4$ giant vortex state. This transition is continuous, i.e. of second order, which can be seen in Fig. 4.2(b) which shows that there is no jump in the free energy.

4.3 PHASE OF THE ORDER PARAMETER

When going around a single vortex the phase of the order parameter changes with 2π. For giant vortex states, we know that the phase of the order parameter will change $L \times 2\pi$ when going around the giant vortex (see Chapter 3). Now, we will investigate the phase of the order parameter in case of a multivortex state. In Figs. 4.8(a-d), the phase of the order parameter in the xy-plane is shown for the $(0, 3)$, the $(1, 5)$, the $(2, 7)$, and the $(3, 8)$-state in a sphere with radius $R = 4\xi$ at magnetic fields $H/H_{c2} = 0.65$, 0.65, 1.15, and 1.27, respectively. Notice that these multivortex states are (meta-)stable at the considered magnetic field values. Red regions correspond with phases near 2π, while blue regions corresponds with phases near zero. Let us first

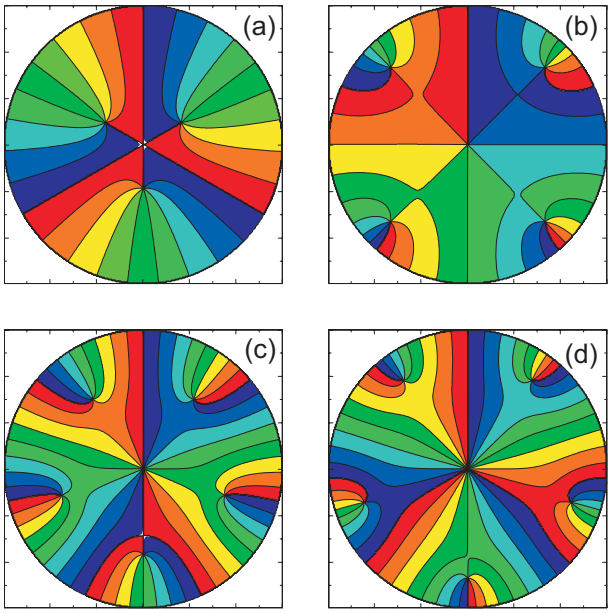

Fig. 4.8 Contour plots of the phase of the order parameter in the xy-plane of a sphere with radius $R = 4\xi$ for the $(0,3),(1,5),(2,7),(3,8)$-states $H/H_{c2} = 0.65, 0.65, 1.15, 1.27$.

consider the $(0,3)$-state in Fig. 4.8(a). When encircling the sphere near the boundary, we find that the phase changes 3 times with 2π. This means that the total vorticity is zero. When encircling the center of the sphere, the phase remains almost zero (or 2π which means the same). So, there is no vortex in the center. The 3 vortices are clearly on a shell around the center of the sphere. When encircling such vortex, the phase changes clearly with 2π, which means that the vortex is singly quantized. From Fig. 4.8(b) we know that the $(1,5)$-state has total vorticity 5. It contains one singly quantized vortex in the center and 4 single vortices on a shell. The $(2,7)$-state (Fig. 4.8(c)) has total vorticity 7, a giant vortex with vorticity $L = 2$ in the center and 5 singly quantized vortices on a shell. Fig. 4.8(d) shows the $(3,8)$-state, which consists of a giant vortex with $L = 3$ in the center and 5 single vortices on a shell. The total vorticity is 8.

Figs. 4.9(a-d) show the phase of the order parameter for the same situations as Figs. 4.7(a-d), i.e., the $(0,4)$-state in a sphere with radius $R = 4\xi$ at $H = 0.61H_{c2}$, $H = 0.73H_{c2}$, $H = 0.85H_{c2}$, and $H = 1.03H_{c2}$. Also from contour plots of the phase of the order parameter one can see that the vortices move towards the center with increasing magnetic field.

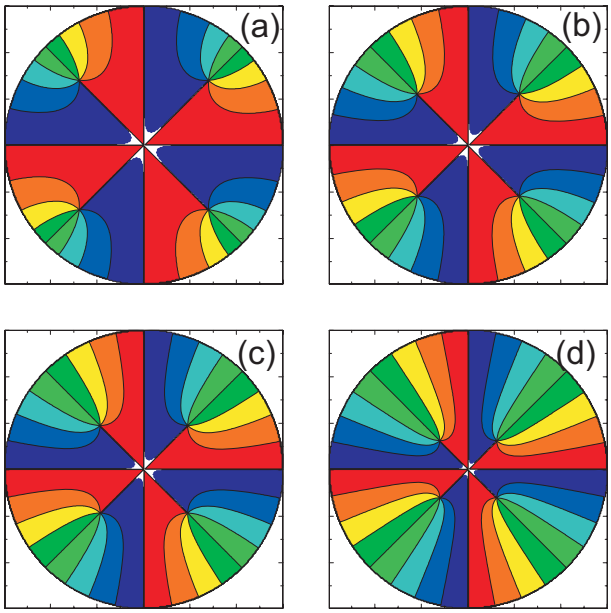

Fig. 4.9 Contour plots of the phase of the order parameter for the same configurations as in Fig. 4.7.

4.4 COEFFICIENTS C_L

The most exciting discovery we found is the new criterion for the stability of multivortex states. For disks, the stability of the multivortex state is checked by the theory given by Schweigert *et al.* [6], by Palacios [1,2], and by Yampolskii *et al.* [3]. In Chapter 2 we adapted this stability criterion to superconducting spheres. For disks, we know that the coefficients C_L are usually complex numbers, but for the two-component state the C_L are real numbers, and the stable states should have the Hessian matrix to be positive. This criterion also works well for the two-component situation in spheres, but now there are still complex coefficients, even for the two-component situation. However for stable states, the coefficients C_L are real, and they are also positive. We have checked this for all of the vortex states studied in our work. This is really a very surprising result, which can be used as a much simpler criterion to determine the stability of the multi-vortex states in mesoscopic spheres.

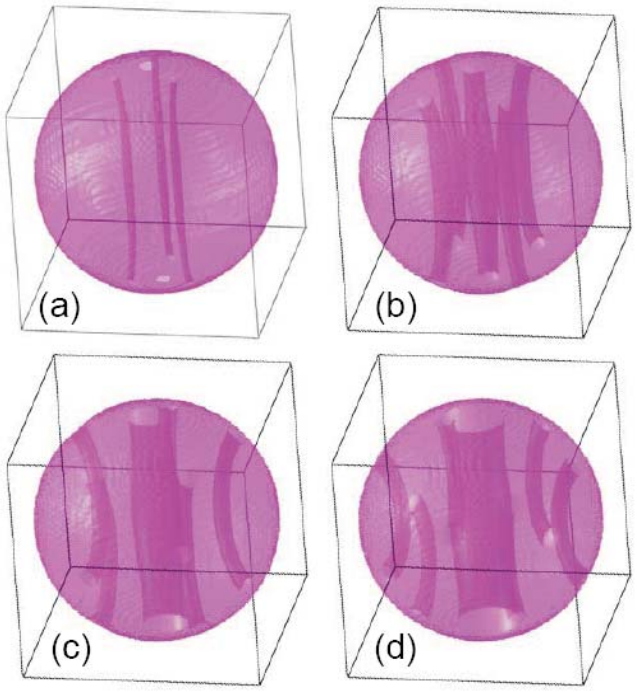

Fig. 4.10 3D figures of the $(0,3),(1,5),(2,7),(3,9)$-state in a superconducting sphere with radius $R = 4\xi$.

4.5 THREE DIMENSIONAL COOPER-PAIR DENSITY

Up to now, our research focused on the Cooper-pair density and the order parameter of the multivortex state in the equator plane of the sphere. Although we only plotted the quantities in the $z = 0$-plane, we always calculated the full three-dimensional order parameter, i.e.,

$$\Psi(\rho,\varphi,z) = C_{L_1}\psi_{L_1}(\rho,z)exp(iL_1\varphi) + C_{L_2}\psi_{L_2}(\rho,z)exp(iL_2\varphi), \qquad (4.1)$$

which we used to calculate the free energy by using equations (2.15) and (2.16) and to check the stability of the different vortex states. Due to the boundary of the sphere, it can be expected that the spatial distribution of the vortices will change when going away from the equator plane, i.e. when considering $z \neq 0$. In this section we will check the three-dimensional distribution of vortices.

As an example, we show in Figs. 4.10(a-d) the three-dimensional distribution of the Cooper-pair density in a superconducting sphere with radius $R = 6\xi$ at $H = 0.70H_{c2}$ for the $(0,3)$, the $(1,5)$, the $(2,7)$, and the $(3,9)$-state.

Notice that the diameters of the vortices in these figures are different from the vortices in the two-dimensional contour plots above. Here we show the isosurfaces where the Cooper-pair density has a fixed but low value. Therefore, we only see the sphere boundary and the "boundaries" of the vortices in Figs. 4.10(a-d). It is clearly shown that the vortices bend towards the boundary of the sphere when moving away from the $z = 0$-plane, except for the (giant) vortex in the center. Fig. 4.10(a) shows the $(0, 3)$-state, where 3 vortices are on a shell in the $z = 0$-plane. It is shown that all vortices bend towards the outer boundary with increasing z. Fig. 4.10(b) shows the $(1, 5)$-state where one vortex is in the center, which is surrounded by 4 vortices on a shell. Now, we see that the central vortex stays along the $\rho = 0$-axis while the other vortices bend outwards. This means that at $z \preceq R$ only the central vortex is still inside the sphere, while the other vortices left the sphere. Figs. 4.10(c,d) show the $(2, 7)$, and the $(3, 9)$-state, where a central giant vortex is surrounded by single vortices. For $z > 0$ the giant vortex remains around the z-axis, while the other vortices move towards the outer boundary. From these figures it is also clear that the radius of the giant vortex increases with vorticity L. Notice further that the radius of the giant vortex is larger around $z = 0$ than for $z > 0$.

Another way to present these results is by plotting two-dimensional contour plots for different values of z. This is done in Fig. 4.11 for the $(2, 7)$-state, which corresponds to the situations of Fig. 4.10(c). Figs. 4.11(a-f) show the results for $z = 0, 1.2, 2.4, 3.6, 4.8, 5.9\xi$, respectively. For $z = 0$ we find a giant vortex with $L = 2$ in the center surrounded by 5 vortices. With increasing z these 5 vortices move towards the outer boundary (see Figs. 4.11(b-d)). Around $z = 4.8\xi$ (see Fig. 4.11(e)) they leave the superconducting sphere. When we further increase z we only find the central giant vortex (see Fig. 4.11(f)).

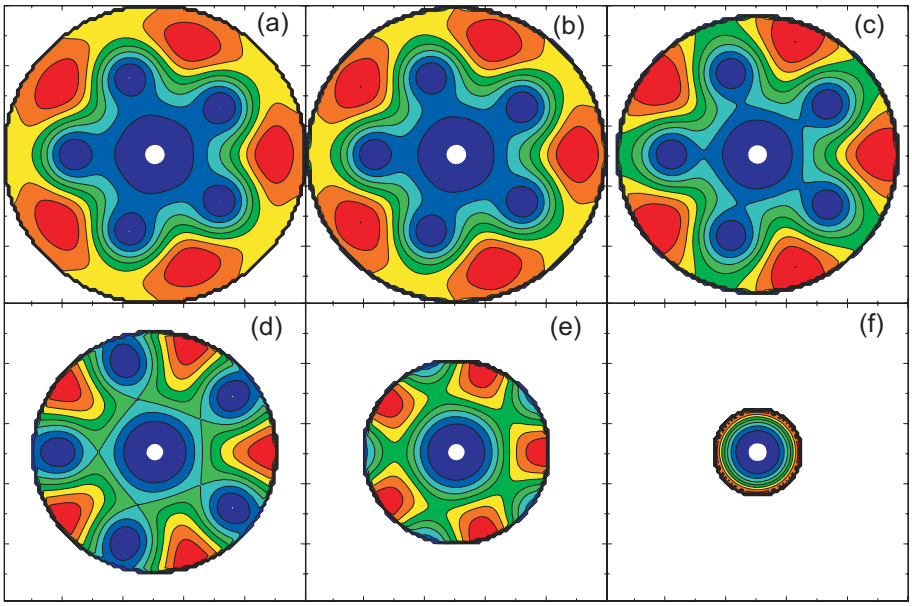

Fig. 4.11 Contour plots of the Cooper-pair density for the configuration of Fig. 4.10(c) for different values of z, i.e. $z = 0, 1.2, 2.4, 3.6, 4.8, 5.9\xi$.

5

Conclusion

We studied theoretically the superconducting states of a mesoscopic superconducting sphere in the presence of a homogeneous magnetic field. The influence of the sphere geometry and the applied magnetic field on the vortex configuration were both investigated for different sphere sizes.

First, we studied the giant vortex states. Solving the GL equation, the density of the cooper-pair, the eigenvalue of the wave function, and the free energy of the giant vortex states are all obtained by the finite element method. And the corresponding phase distribution of these giant vortex states are also obtained numerically. It is found that with increasing sample size, the number of stable vortex states increases. Using the criterion of stability for giant vortex states, we found that the magnetic field range over which there exist stable giant vortices are shorter than the range given by the negative free energy region. Besides, the eigenvalue and wave function of excited states are also investigated. We showed that there are no stable excited vortex states for the mesoscopic sphere situation.

Next, we studied the multi-vortex states, which are obtained by the so called linear combination of the eigenfunction of the linearized GL equation. The Cooper-pair density of the multi-vortex states and stability of the multi-vortex are both obtained. Also, the transitions from giant vortex states to multi-vortex states and from multi-vortex to giant vortex are both found with increasing magnetic field. The dependence of the multi-vortex phase on the magnetic field was found. The dependence of the position of the vortices in a multi-vortex was investigated as function of the magnetic field. Those vortices move closer to each other with increasing field allowing them to coalesce into a giant vortex at a certain magnetic field value. We found the interesting result

that the criterion of stability of a multi-vortex can be simplified. Previously, one requited that of a multi-vortex state constructed out of two giant vortexes, the Hessian matrix should be positive,but in the mesoscopic sphere situation, we found that this criterion can be simplified as the Hessian matrix is real. This was checked for all the stable multi-vortex states studied in this thesis.

References

1. J. J. Palacios, Physica B **256-258**, 610 (1998).
2. J. J. Palacios, Phys. Rev. B **58**, R5948 (1998).
3. S. V. Yampolskii and F. M. Peeters, Phys. Rev. B **62**, 9663 (2000).
4. W. Meissner and R. Ochsenfeld, Naturwiss. **21**, 787 (1933).
5. V. A. Schweigert and F. M. Peeters, Phys. Rev. B **57**, 13817 (1998).
6. V. A. Schweigert and F. M. Peeters, Phys. Rev. Lett. **83**, 2409 (1999).
7. L. D. Landau and E. M. Lifshitz, *Statistical Physics*, 3rd edn., part 1 (Pergamon Press, Oxford, 1980).
8. V. A. Schweigert, F. M. Peeters, and P. S. Deo, Phys. Rev. Lett. **81**, 2783 (1998).
9. A. A. Abrikosov, Sov. Phys. JETP **5**, 1175 (1957).
10. Q. Du, Journal of Mathematical Physics **46**, 095109 (2005).
11. J. G. Bednorz and K. A. Müller, Z. Phys. B **64**, 189 (1986).
12. A. Schilling, M. Cantoni, J. D. Guo, and H. R. Ott, Nature **363**, 56 (1993).

13. J. Bardeen, L. N. Cooper, and J. R. Schrieffer, Phys. Rev. **108**, 1175 (1957).

14. S. N. Putilin, E. V. Antipov, A. M. Abakumov, M. G. Rozova, K. A. Lokshin, D. A. Pavlov, A. M. balagurov, D. V. Sheptyakov, and M. Marezio, Physica C **338**, 52 (2000).

15. Q. Du, SIAM. Rev, **34**,54, (1992).

16. C. Kittel, Introduction to Solid State Physics (John Wiley & Sons, New York, 1996).

17. L. N. Cooper, Phys. Rev. **104**, 1189 (1956).

18. P. G. de Gennes, *Superconducting of Metals and Alloys* (Benjamin, New York, 1966).

19. D. Saint-James, G. Sarma, and E. J. Thomas, *Type II Superconductivity* (Pergamon Press, Oxford, 1969).

20. P. Singha Deo, V. A. Schweigert, F. M. Peeters, and A. K. Geim, Phys. Rev. Lett. **79**, 4653 (1997).

21. L. P. Gor'kov, Sov. Phys. JETP **9**, 1364 (1959).

22. V. V. Schmidt, P. Müller, and A. V. Ustinov, *The Physics of Superconductors: Introduction to Fundamentals and Applications* (Springer-Verlag, Berlin Heidelberg, 1997).

23. V. L. Ginzburg and L. D. Landau, Zh. Eksperim. i. Teor. Fiz. **20**, 1064 (1950).

24. B. Baelus, *Vortexmatter in Mesoscopic Superconductors* (Ph.D thesis, 2002)

25. M. Tinkham, *Introduction to Superconductivity* (McGraw Hill, New York, 1975).